Combined Effects of Midlevel Dry Air and Vertical Wind Shear on Tropical Cyclone Development. Part I: Downdraft Ventilation🖉

JOSHUA J. ALLAND,[a] BRIAN H. TANG,[b] KRISTEN L. CORBOSIERO,[b] AND GEORGE H. BRYAN[a]

[a] *National Center for Atmospheric Research, Boulder, Colorado*
[b] *Department of Atmospheric and Environmental Sciences, University at Albany, State University of New York, Albany, New York*

ABSTRACT: This study examines how midlevel dry air and vertical wind shear (VWS) can modulate tropical cyclone (TC) development via downdraft ventilation. A suite of experiments was conducted with different combinations of initial midlevel moisture and VWS. A strong, positive, linear relationship exists between the low-level vertical mass flux in the inner core and TC intensity. The linear increase in vertical mass flux with intensity is not due to an increased strength of upward motions but, instead, is due to an increased areal extent of strong upward motions ($w > 0.5\ \mathrm{m\ s^{-1}}$). This relationship suggests physical processes that could influence the vertical mass flux, such as downdraft ventilation, influence the intensity of a TC. The azimuthal asymmetry and strength of downdraft ventilation is associated with the vertical tilt of the vortex: downdraft ventilation is located cyclonically downstream from the vertical tilt direction and its strength is associated with the magnitude of the vertical tilt. Importantly, equivalent potential temperature of parcels associated with downdraft ventilation trajectories quickly recovers via surface fluxes in the subcloud layer, but the areal extent of strong upward motions is reduced. Altogether, the modulating effects of downdraft ventilation on TC development are the downward transport of low–equivalent potential temperature, negative-buoyancy air left of shear and into the upshear semicircle, as well as low-level radial outflow upshear, which aid in reducing the areal extent of strong upward motions, thereby reducing the vertical mass flux in the inner core, and stunting TC development.

KEYWORDS: Atmosphere; Tropical cyclones; Convective-scale processes; Numerical analysis/modeling

1. Introduction

a. Effects of vertical wind shear on tropical cyclone development

Vertical wind shear (VWS) strongly influences tropical cyclone (TC) intensity change (DeMaria and Kaplan 1994). As a result, VWS is an important parameter in statistical intensity prediction models and operational TC intensity forecasts (DeMaria et al. 2005; Knaff et al. 2005; Finocchio and Majumdar 2017b), and a better understanding of how VWS affects TC development is crucial to intensity forecast error reduction (DeMaria et al. 2005).

VWS tilts a TC vortex and causes differential vorticity advection, which acts to increase low-level convergence through quasigeostrophic forcing, upward motion along raised isentropes (Jones 1995, 2000; Frank and Ritchie 1999), and a downshear redistribution of convection (Nguyen and Molinari 2012; Finocchio et al. 2016). Convection is suppressed on the upshear side of the storm (Marks et al. 1992; Chen et al. 2006), resulting in a wavenumber-1 asymmetry in vertical motion. This pattern can be viewed as a balanced response to vortex tilt (Reasor et al. 2013), with the magnitude of the tilt corresponding to the strength (Rogers et al. 2003), height, and depth (Finocchio et al. 2016; Finocchio and Majumdar 2017a,b) of the VWS. Updrafts generally initiate downshear right (DR) and convection

matures downshear left (DL), as the updrafts rise within the cyclonic circulation (Frank and Ritchie 1999; DeHart et al. 2014). This shear-induced convective pattern has been confirmed in observational (Reasor et al. 2000; Corbosiero and Molinari 2002; Chen et al. 2006; Reasor and Eastin 2012; Reasor et al. 2013; DeHart et al. 2014) and modeling (DeMaria 1996; Wang and Holland 1996; Frank and Ritchie 2001) studies.

The tilt and associated convective asymmetries are generally considered inhibitive for intensification. First, the balanced mass field of a tilted potential vorticity (PV) anomaly requires an increase in the midlevel temperature anomaly above the low-level vortex center. This process acts to stabilize the column above the center and inhibit storm development (DeMaria 1996). Second, Frank and Ritchie (2001) described VWS as weakening the TC warm core from the top down (Kwon and Frank 2008). From this perspective, VWS erodes the warm core at upper levels and, through hydrostatic arguments, raises the minimum pressure of the TC.

Despite recent advances in the understanding of how VWS impacts TC development, open questions remain. For example, what physical processes impact the azimuthal variation in convection; and how does this variation modulate TC development? This study investigates these questions.

b. Combined effects of dry air and VWS on TC development

With no mean flow, dry air can stunt TC development if the dry air is able to penetrate the inner core (Braun et al. 2012) by reducing the net upward vertical mass flux, frictional convergence, and the inward transport of absolute angular momentum in the boundary layer (Montgomery and Smith 2014; Tang et al. 2016;

🖉 Supplemental information related to this paper is available at the Journals Online website: https://doi.org/10.1175/JAS-D-20-0054.s1.

Corresponding author: Joshua J. Alland, jalland@ucar.edu

Alland et al. 2017). When working together with VWS, TC development is further stunted. Ventilation, defined as the flux of low–equivalent potential temperature (θ_e) environmental air into the TC inner core (Simpson and Riehl 1958; Riemer et al. 2010; Tang and Emanuel 2012a), acts counter to the TC heat engine and inhibits development (Cram et al. 2007; Marín et al. 2009; Tang and Emanuel 2012b; Munsell et al. 2013). Tang and Emanuel (2010) used a theoretical framework to demonstrate that increased ventilation reduces TC intensity and, for a large enough ventilation, results in weakening TCs. Thus, developing disturbances tend to exist in environments of low VWS and low midlevel θ_e deficits (Tang and Emanuel 2012b; Komaromi 2013). Prior research has investigated the effects of dry air and VWS on mature TCs, described next in more detail, but the effects of ventilation earlier during development have been less studied.

Previous studies have documented different ventilation pathways and their effects on TC intensification. Dry air can ventilate the subcloud layer (low-level pathway) via convective downdrafts (Riemer et al. 2010). Dry air can also ventilate midlevels (midlevel pathway) and reduce the θ_e of rising parcels in the eyewall. For both of these pathways, dry air originates from midlevels (Tang and Emanuel 2010). The third pathway by which the TC heat engine can be frustrated is the upper-level pathway, described previously, wherein VWS acts to weaken a TC from the top down through the erosion of the upper-level warm core (Frank and Ritchie 2001; Kwon and Frank 2008). Tang and Emanuel (2012a) argued that upper-level ventilation is inefficient at frustrating the TC heat engine since the radial gradient of θ_e is weaker at upper levels.

The low-level pathway involves the flux of low-θ_e air into the subcloud layer from convective downdrafts (Tang and Emanuel 2012a) or rainband activity (Barnes et al. 1983; Powell 1990; Hence and Houze 2008; Didlake and Houze 2009). A series of studies considered the location of downdrafts with respect to VWS (Riemer et al. 2010, 2013; Riemer and Montgomery 2011). The VWS acts to initiate upward motion downshear and downward motion upshear. The upward motion in these studies resembles the stationary band complex first documented in Willoughby et al. (1984). Riemer and Montgomery (2011), using a simple kinematic model, suggested that the downdrafts that bring low-θ_e air into the subcloud layer are associated with helically rising updrafts and convection in the downshear semicircle. Rainfall into unsaturated air below results in evaporative cooling and a quasi-steady location of downdrafts out to a radius of about 150 km (Nguyen and Molinari 2012). Underneath this persistent area of downdrafts, a reservoir of low-θ_e air is transported inward by the low-level inflow. This reservoir of low-θ_e air increases with the magnitude of VWS (Riemer et al. 2010, 2013). If surface fluxes are not able to recover the θ_e of the inflowing parcels, the air feeding into eyewall updrafts may have a lower mean θ_e (Riemer et al. 2010) and reduced net upward vertical mass flux, which are associated with vortex spindown (Smith and Montgomery 2015) and a weakening of the TC heat engine, suggesting that this pathway may be an important modulating effect on TC intensity in VWS (Riemer et al. 2010, 2013). Note, however, that enhanced surface fluxes into the low-θ_e air may counteract

these debilitating effects (Tang and Emanuel 2012b; Tao and Zhang 2014; Juračić and Raymond 2016; Gao et al. 2017).

c. Purpose of this study

The low- and midlevel ventilation pathways are described in the literature, but the importance of each pathway and the environments under which they may operate remain unclear (Riemer and Laliberté 2015), especially for weak TCs. Previous literature has studied these ventilation pathways from an axisymmetric perspective (Tang and Emanuel 2012a), but how important are these ventilation pathways in a three-dimensional framework? Previous literature has relied on case studies (Cram et al. 2007) or modeling studies with differing magnitudes of VWS (Riemer et al. 2010; Riemer and Montgomery 2011), but the importance of these ventilation pathways may depend on the magnitude of the VWS and the thermodynamic environment, particularly the midlevel moisture. Therefore, how important are these ventilation pathways in a moisture–VWS bivariate parameter space? What are their three-dimensional structures, and how do they modulate convection and TC development? A better understanding of the different ventilation pathways on TC development is vital to better forecast TC intensity change.

This paper concentrates on low-level ventilation, while Alland et al. (2021, hereafter Part II) concentrates on midlevel ventilation. We introduce an important change in terminology from previous studies: To better associate low-level ventilation with its physical phenomenon, this manuscript refers to the downward transport of low-θ_e air as "downdraft ventilation." Similarly, Part II refers to the radial transport of low-θ_e air, which does not have to be confined to midlevels, as "radial ventilation."

Section 2 presents the model setup and a bivariate parameter space of model experiments. Section 3 shows the effects of dry air and VWS on TC evolution. Section 4 presents a linear relationship between the vertical mass flux in the inner core and TC development, demonstrating that processes that affect the vertical mass flux, such as downdraft ventilation, may affect TC development. This result motivates the investigation of downdraft ventilation by examining its three-dimensional structure in section 5 and its effects on convection in section 6. Section 7 summarizes this study with a conceptual diagram.

2. Methodology

Cloud Model 1 (CM1; Bryan and Fritsch 2002) is used to perform the experiments. The model is set up in three dimensions on an f plane with a Coriolis parameter set to $5 \times 10^{-5}\,\mathrm{s}^{-1}$. The horizontal grid spacing is 3 km within 500 km of the domain center, beyond which the grid stretches incrementally from 3 to 16 km at the outermost portion of the domain. The total size of the domain is 1536 km × 1536 km. The vertical grid has 59 levels with spacing that stretches from 50 to 500 m in the lowest 5500 m, above which the spacing remains 500 m. The model top is 25 km. Parameterization schemes employed are listed in Table 1.

Nine experiments were conducted. Each experiment is initialized with the moist tropical temperature profile of Dunion (2011), has a sea surface temperature of 29°C, and the initial

TABLE 1. Parameterization schemes used in the CM1 simulations.

	Parameterization
Microphysics	Morrison double-moment (Bryan and Morrison 2012)
Radiation	RRTMG longwave and shortwave (Iacono et al. 2008)
PBL	Yonsei University (Hong et al. 2006)
Surface fluxes	Bulk aerodynamic formulas (Fairall et al. 2003; Donelan et al. 2004; Drennan et al. 2007)
Turbulence	Bryan and Rotunno (2009) and Bryan (2012)

vortex described in Rotunno and Emanuel (1987). The initial vortex has a maximum wind speed of $12 \, \mathrm{m \, s^{-1}}$ that decreases linearly with height, a radius of maximum wind (RMW) of 82.5 km, and a radius of zero wind of 412.5 km. The initial temperature field is in thermal wind balance with the initial vortex.

Each experiment differs in the combination of initial relative humidity (RH) and VWS above 850 hPa. RH profiles are set to a constant value above 850 hPa in increments of 30%, ranging from a very moist (RH = 80%) to dry (RH = 20%) profile. The initial moisture (RH) below 850 hPa is set to the Dunion moist tropical profile (Dunion 2011) and is the same across experiments (Fig. 1a).

VWS magnitudes are set to a constant value, in increments of $5 \, \mathrm{m \, s^{-1}}$, ranging from 0 to $10 \, \mathrm{m \, s^{-1}}$. The middle and upper ends of this range encompass moderate VWS (Rios-Berrios and Torn 2017), which is associated with greater uncertainty in the timing of TC intensification (Zhang and Tao 2013; Tao and Zhang 2014). The VWS is a linearly increasing, westerly wind from 850 to 200 hPa, with no wind at and below 850 hPa, and a constant wind speed above 200 hPa (Fig. 1b).

To include VWS, a large-scale pressure gradient term is added to the horizontal momentum equations. This technique, described by Nolan and Rappin (2008) and implemented in several studies (Moeng 1984; Skamarock et al. 1994; Nolan 2011; Zhang and Tao 2013; Finocchio and Majumdar 2017a; Onderlinde and Nolan 2017), adds VWS without including a meridional temperature gradient. The large-scale pressure gradient term accounts for the pressure force that would be present to balance the mean VWS if a temperature gradient existed. The appendix has a detailed explanation of this implementation in CM1.

There is no VWS during the first 12 h, allowing each experiment to spin up a realistic vortex with convection. After 12 h, the desired wind profiles in Fig. 1b are nudged in at each grid point (Fig. 1c). The desired wind profiles are fully implemented by 24 h and remain roughly constant.

CM1 uses a moving domain that centers the grid on the TC center so that the bulk of the TC circulation always remains in the high-resolution region of the domain. The TC center is determined by smoothing the surface pressure field, using a two-dimensional Gaussian filter, and locating the minimum of the smoothed pressure.

The three different RH and VWS magnitudes give a total of nine experiments, and each experiment was integrated forward 96 h. Hereafter, the experiments are labeled as RH*XX*S*YY*, where *XX* and *YY* are the magnitudes of the initial RH and
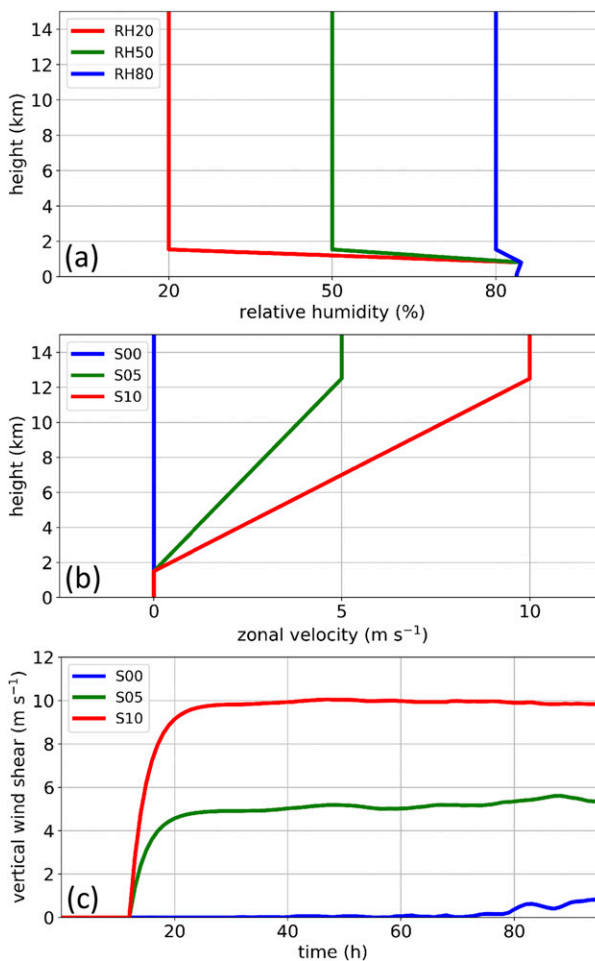

FIG. 1. (a) Vertical profile of relative humidity for RH magnitudes of 20% (red), 50% (green), and 80% (blue). (b) Vertical profile of the zonal wind for VWS magnitudes of 0 (blue), 5 (green), and 10 (red) $\mathrm{m \, s^{-1}}$. (c) Time series of the VWS magnitude. The large-scale wind profiles are nudged toward the VWS magnitudes in (b) starting at 12 h, with a relaxation time scale of 3 h.

VWS, respectively (e.g., RH20S05 refers to the experiment with 20% RH above 850 hPa and $5 \, \mathrm{m \, s^{-1}}$ of deep-layer vertical wind shear). Experimental sets, such as the three experiments with the same initial RH or VWS magnitude, are labeled as RH*XX* or S*YY*, respectively.

3. Evolutions of the TCs

a. Maximum 10-m wind speed

The evolutions of the maximum, azimuthally averaged, 10-m wind speed (Vmax) for the RH20, RH50, and RH80 experimental sets are presented in Figs. 2a–c, respectively. Note that "development" is comprised of a nonintensifying stage, followed by an early intensification stage of a TC's life cycle. For the RH20 experimental set, no development occurs during the first 36 h. After 36 h, RH20S05 develops first, followed by RH20S00, suggesting that some VWS may be beneficial for
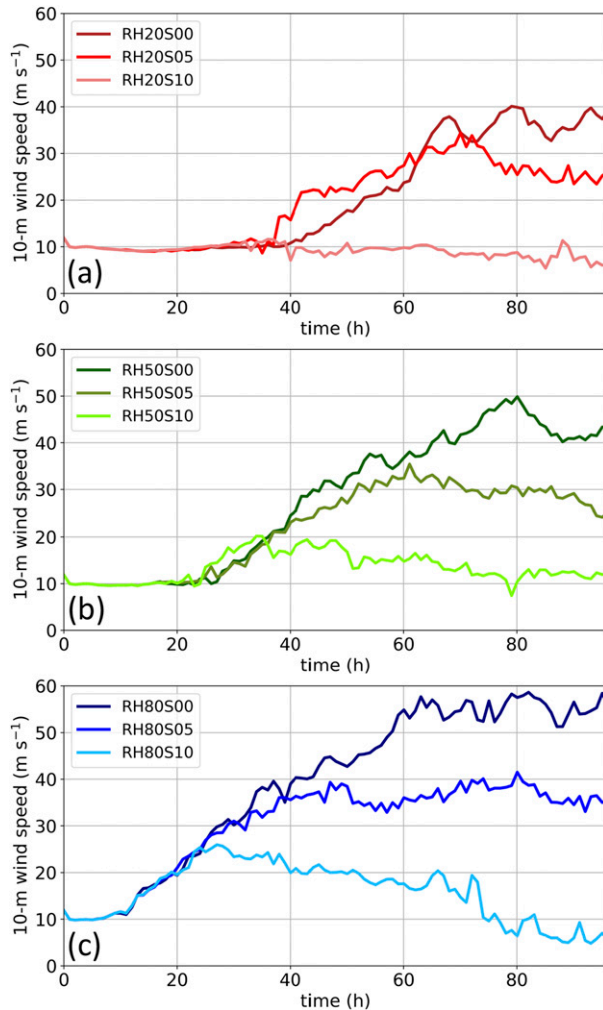
FIG. 2. Time series of the maximum azimuthally averaged 10-m wind speed (m s^{-1}) for the (a) RH20, (b) RH50, and (c) RH80 experimental sets.

initial development (Bracken and Bosart 2000). With time, Vmax for RH20S00 reaches 40 m s^{-1}, which is higher than RH20S05 (33 m s^{-1}), suggesting that VWS ultimately stunts development for RH20S05. RH20S10 fails to develop for the entire simulation due to the unfavorably low midlevel RH and large VWS. For the RH50 experimental set, no development occurs during the first 22 h. After 22 h, all experiments begin to develop at roughly the same rate. After 36 h, RH50S00 develops more quickly than RH50S05, while RH50S10 slowly decays. For the RH80 experimental set, moist midlevels facilitate quicker development compared to the RH50 and RH20 sets. Vmax for each experiment reaches approximately 25 m s^{-1} by 24 h, at which time the VWS is fully implemented. After 24 h, RH80S00 develops more quickly than RH80S05, while RH80S10 slowly decays, similar to the RH50 experimental set. The comparison between Vmax for each experimental set suggests that a VWS magnitude of 5 m s^{-1} is high enough to stunt development, while a VWS magnitude of 10 m s^{-1} is high

enough to inhibit development, at least in these sets of experiments.

The variability in the timing and rate of development across the bivariate parameter space in Fig. 2 suggests that TC development is sensitive to the magnitudes of midlevel humidity and VWS. This high variability motivates the investigation of ventilation pathways to determine the physical mechanisms behind the large variability in development time and rate.

b. Vertical tilt of the vortex

VWS tilts the TC vortex and affects the azimuthal distribution of convection (Corbosiero and Molinari 2002), which is potentially modulated by ventilation. To determine how the three-dimensional structure of downdraft ventilation is ultimately influenced by vertical tilt, the magnitude and direction of the vertical tilt are diagnosed for each experiment. The center position at each vertical level is determined by finding the minimum of the smoothed pressure, and vertical tilt is calculated from the surface to a height of 6 km. The time evolution of the vertical tilt magnitude is presented in Figs. 3a and 3b, and the planar evolution of the tilt magnitude and direction is shown in Figs. 3c and 3d. Note that experiments with the same magnitude of VWS are presented together. The S00 experimental set is not shown since the tilt magnitude is small (usually under 2 km) and fluctuates about all azimuths around the TC low-level center.

Figure 3 shows that the vertical tilt in these simulations is modulated by the humidity. For the S05 experimental set (Fig. 3a), the vertical tilt generally increases after VWS is introduced at 12 h. RH20S05 has the largest tilt of the S05 experiments, increasing rapidly from near zero at 12 h to about 23 km by 30 h. After 30 h, a sharp decline occurs, coincident with an increase in Vmax (Fig. 2a), and the tilt remains quasi steady at about 3 to 5 km from 50 to 96 h. RH50S05 has a tilt that increases at the same rate as RH20S05 from 12 to 20 h, but the tilt peaks at 11 km by 20 h and generally decreases until 55 h. During this period of tilt reduction, the TC steadily develops (Fig. 2b). RH80S05 does not have a sharp tilt increase after 12 h, but increases incrementally from 1 to 3 km by the end of the simulation. Comparing the tilt magnitude evolutions of the S05 experiments suggests that TCs in a drier environment are less resilient to VWS (i.e., they develop a larger vertical tilt). The planar evolution (Fig. 3c) shows a tilt direction downshear and DL for each experiment. The tilt direction of RH20S05 and RH50S05 rotates cyclonically as the vertical tilt is reduced, agreeing with previous work that development occurs consistent with this tilt evolution (Zhang and Tao 2013; Onderlinde and Nolan 2014; Finocchio et al. 2016; Rios-Berrios et al. 2018).

For the S10 experimental set (Fig. 3b), the tilt magnitudes are much larger. During the first 40 h, RH20S10 has the largest tilt increase, reaching about 60 km before decreasing to under 20 km by 52 h. The sharp tilt decrease is likely the result of the center position changing because the TC is weak (Fig. 2a), and the center is ill-defined in this simulation. RH50S10 follows the tilt increase of RH20S10 during the first 20 h, after which the tilt slowly decreases until 48 h. During the period of tilt reduction, the intensity slowly increases (Fig. 2b). RH80S10 has a slower increase in vertical tilt from 24 to 50 h compared to the
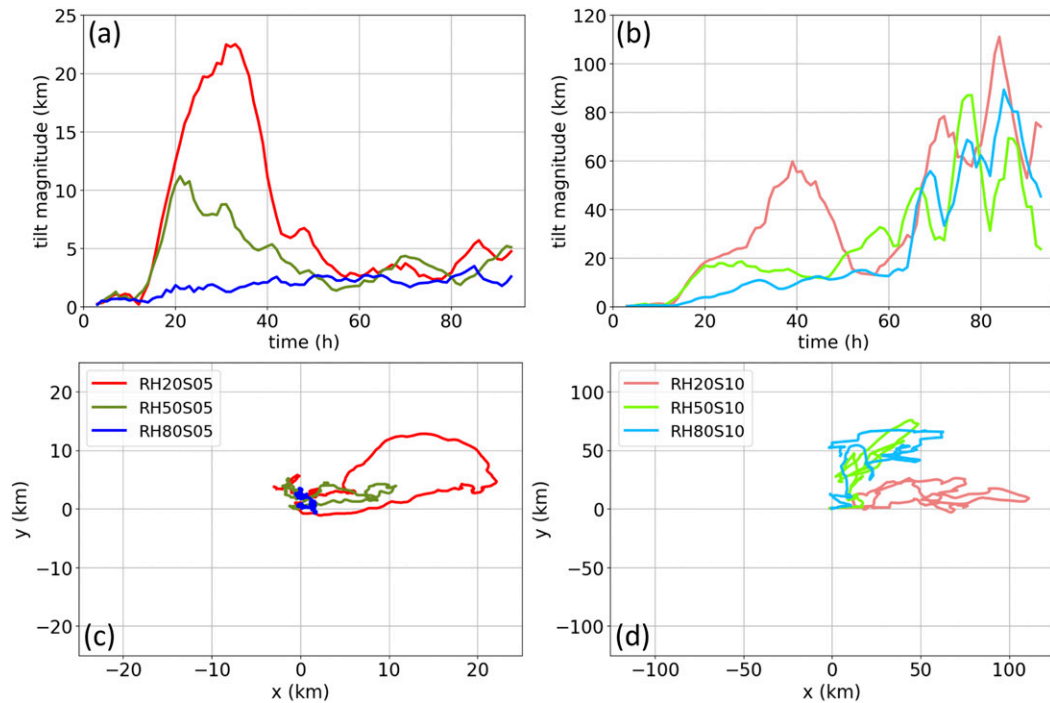
FIG. 3. (top) Time series of the vertical tilt magnitude (km) from the surface to 6 km for the (a) S05 and (b) S10 experimental sets. (bottom) Planar plots of the vertical tilt evolution relative to the surface center for the (c) S05 and (d) S10 experimental sets. A 6-h running mean was applied to reduce the noise. Note that the scaling on the ordinates is roughly 5 times greater for the S10 experimental set compared to the S05 experimental set.

other experiments, likely because this TC is stronger, and more resilient to VWS, compared to the other S10 simulations; however, this TC weakens slowly during this time period (Fig. 2c). After 52 h, all three experiments have large fluctuations in the vertical tilt. During this time period, all TCs have intensities at or below $20 \, \mathrm{m \, s^{-1}}$, and all weaken to an intensity of roughly $10 \, \mathrm{m \, s^{-1}}$ by the end of the simulation (Fig. 2). This result suggests that a VWS magnitude of $10 \, \mathrm{m \, s^{-1}}$ is large enough to consistently weaken TCs in these simulations, despite RH50S10 and RH80S10 being more intense than RH20S10 around 30 h. The planar evolution of tilt direction (Fig. 3d) shows that the tilt of RH20S10 is consistently downshear, while the other two experiments have tilts consistently DL. This difference may be due to increased convection (shown next) and more humid environments in RH50S10 and RH80S10, compared to RH20S10, which can facilitate vortex precession (Tao and Zhang 2014). Similar to the S05 experiments, the S10 experiments suggest that TCs in a drier environment are less resilient to VWS, at least initially.

The remainder of this study will concentrate on comparing experiments with the same magnitude of RH (the RH*XX* experimental sets), as separated in Fig. 2. Clear "bifurcation points" in intensity occur for each experimental set in Fig. 2, providing justified time periods to investigate physical processes that may be modulating the bifurcation in each experimental set. In contrast, experimental sets with the same VWS magnitude do not have similar bifurcation points, likely because these experiments have different time periods over which the near

environment moistens. Hereafter, figures that are time averaged begin at the bifurcation point, namely, 36 h for RH20 and RH50, and 24 h for RH80, and extend for 12 h (Fig. 2). This time period, called the "bifurcation time period," compares TCs when ventilation may be influencing the intensity differences.

c. Reflectively structure

To diagnose how the vertical tilt is associated with the structure of convection during the bifurcation time period, Fig. 4 presents reflectivity at a height of 1 km at the beginning of the bifurcation time period. For reference, the numbers at the top right of each panel list the percent of points in the inner 75 km with reflectivity greater than 20 dB*Z*, which is a simple proxy for precipitation coverage, as well as the vertical tilt magnitude and direction between the surface and a height of 6 km, time averaged during the bifurcation time period. For RH20S00 (Fig. 4a), convection is disorganized, associated with the weak intensity at this time (Fig. 2a), and located at all azimuths about the TC center. For RH20S05 (Fig. 4b), convection is concentrated almost exclusively in the downshear semicircle. This experiment initially develops more quickly than RH20S00 (Fig. 2a), likely due to the more organized convection. For RH20S10 (Fig. 4c), convection is concentrated solely downshear in a narrow azimuthal sector and farther from the TC center compared to RH20S05.

The TCs in the RH50 experimental set (Figs. 4d–f) are stronger and more organized than the RH20 set. For RH50S00, the TC has a ring of reflectivity greater than 40 dB*Z* about the
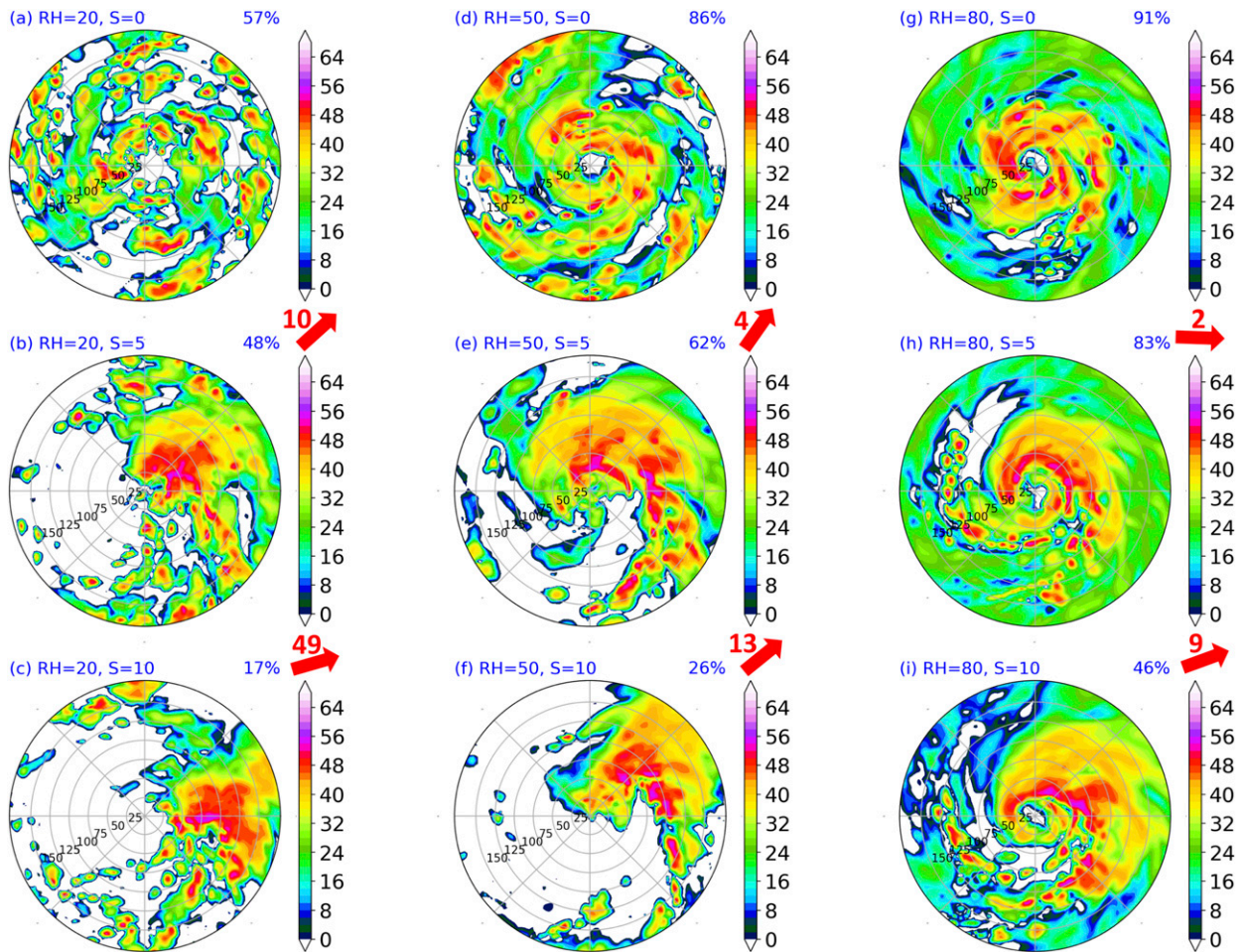
FIG. 4. Model-derived reflectivity (dBZ) at a height of 1 km across the bivariate parameter space. The reflectivity is plotted (a)–(f) at 36 h for the RH20 and RH50 experimental sets and (g)–(i) at 24 h for the RH80 experimental set. These times represent the beginning of the bifurcation time period. The percentage of points in the inner core with reflectivity greater than 20 dBZ is given by the value at the top right of each panel. The vertical tilt magnitude (km) and direction between the surface and a height of 6 km, time averaged during the bifurcation time period, are represented by the red number and arrow, respectively, for the experiments with VWS at the top right of each panel. Range rings are every 25 km.

center. For RH50S05, convection within the inner 40 km is displaced DL and wraps around to the upshear-left (UL) and upshear-right (UR) quadrants. High reflectivity also exists in the DR quadrant, albeit at larger radii of about 60 to 120 km from the center. The convective structure resembles the stationary band complex and principal rainband of Willoughby et al. (1984). A notch of near-zero reflectivity begins at radii greater than 100 km in the UL quadrant and wraps inward to a radius of roughly 40 km within the DR quadrant. For RH50S10, high reflectivity in the inner 40 km is mostly concentrated in the DL quadrant, with less coverage into the UL quadrant compared to RH50S05. A similar, but more extensive, area of near-zero reflectivity encompasses most of the right-of-shear quadrants, and extends slightly into the DL quadrant at radii between 60 and 80 km. As will be shown in section 5, this notch is associated with downdraft ventilation and affects the distribution of convection.

For the RH80 experimental set (Figs. 4g–i), the stronger TCs are associated with a ring of convection about the TC center.

The ring becomes more asymmetric as the VWS increases, with weaker reflectivity in the UL, UR, and DR quadrants. Additionally, rainband activity is more apparent downshear and right of shear between radii of 60 and 100 km as the VWS increases. A notch of near-zero reflectivity appears in RH80S05 and RH80S10 in the UL and UR quadrants, but the area is less extensive than in the RH50 experimental set. This notch gets closer to the TC center for RH80S10 compared to RH80S05.

The structure of reflectivity closely matches TC structure under VWS documented in previous work (e.g., Onderlinde and Nolan 2017), providing confidence that the CM1 setup can capture the evolution of a TC in a vertically sheared environment. As VWS increases, the vertical tilt magnitude increases (red values associated with the arrows) and the area of convection in the inner 75 km decreases, as convection is predominantly downshear and DL. With lower initial RH magnitudes, the weaker TCs
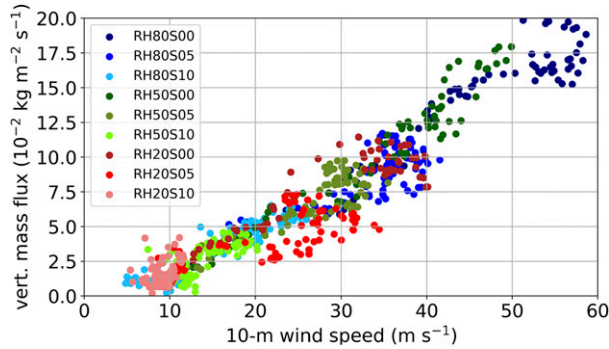
FIG. 5. Vertical mass flux ($\times 10^{-2}$ kg m^{-2} s^{-1}) vs the maximum azimuthally averaged 10-m wind speed (m s^{-1}) across the bivariate parameter space. The vertical mass flux is averaged in a volume from the surface to a height of 1 km, and within 75 km of the TC center. Dots are plotted every hour.

are associated with more asymmetric convection that is farther from the core.

4. Relationship between the vertical mass flux and TC intensity

The previous section demonstrated that convection becomes more asymmetric as the magnitude of VWS increases, with high reflectivity encompassing a smaller azimuthal area around the TC center. But, does a relationship exist between the area and strength of convection, and the intensity of a TC? An increased understanding of this potential relationship would help to better connect the influence of ventilation pathways, which can affect the vertical mass flux, on TC intensity.

Figure 5 presents a scatterplot of the maximum, azimuthally averaged, 10-m wind speed (i.e., TC intensity) versus the vertical mass flux for each experiment in the bivariate parameter space. The vertical mass flux represents an average within the inner 75 km from the surface to 1 km. Each dot represents an hour within the span of each 96-h simulation. A strong linear relationship exists between these two variables: a larger vertical mass flux is associated with a stronger intensity. Note that this linear relationship also exists when the vertical mass flux is

averaged over various layers, such as from 3 to 10 km and from 5 to 10 km (not shown), suggesting that this linear relationship is associated with the development of a deep secondary circulation. Expanding the vertical mass flux to larger areas, such as the inner 100 or 300 km, does not produce a clear linear relationship, and a time-lag correlation between vertical mass flux and intensity shows that they vary together (not shown). Averaging over different radii and a dynamic radius were tried, such as 2.5 times the RMW, but the linear relationship was strongest for a fixed radius of 75 km. The relationship using a dynamic radius was not as strong, likely because the RMW frequently changes from one time step to another for the weak TCs in these experiments. The strong linear relationship suggests that the vertical mass flux within the inner 75 km is linked to TC intensity in these simulations. Therefore, physical processes influencing the vertical mass flux in the inner 75 km, such as ventilation, may influence the intensity of a TC. For these reasons, the inner core is hereafter defined as the inner 75 km with respect to the low-level center.

To determine if a certain range of vertical velocity magnitudes control the linear increase in vertical mass flux with TC intensity, Fig. 6 shows the cumulative vertical mass flux as a function of vertical velocity in the inner 75 km. These panels have been time averaged during the bifurcation time period, and the vertical mass flux has been summed in the lowest 1 km. For the RH20 experimental set (Fig. 6a), vertical motions less than 0.5 m s^{-1} contribute, roughly, the same vertical mass flux magnitude. For vertical velocities greater than 0.5 m s^{-1}, RH20S05 has more frequent strong upward motions contributing to a greater vertical mass flux compared to RH20S00 and RH20S10. The larger vertical mass flux of RH20S05 is associated with a stronger intensity during the bifurcation time period (Fig. 2a), suggesting that some VWS is beneficial for initial development (Bracken and Bosart 2000).

The RH50 experimental set (Fig. 6b) shows a similar pattern as the RH20 set: upward motions less than 0.5 m s^{-1} contribute to a similar vertical mass flux between experiments. RH50S00 and RH50S05 have more frequent upward motions greater than 0.5 m s^{-1}, compared to RH50S10, which result in a greater total vertical mass flux for these experiments. Note that the difference in the vertical mass flux between RH50S00 and RH50S05
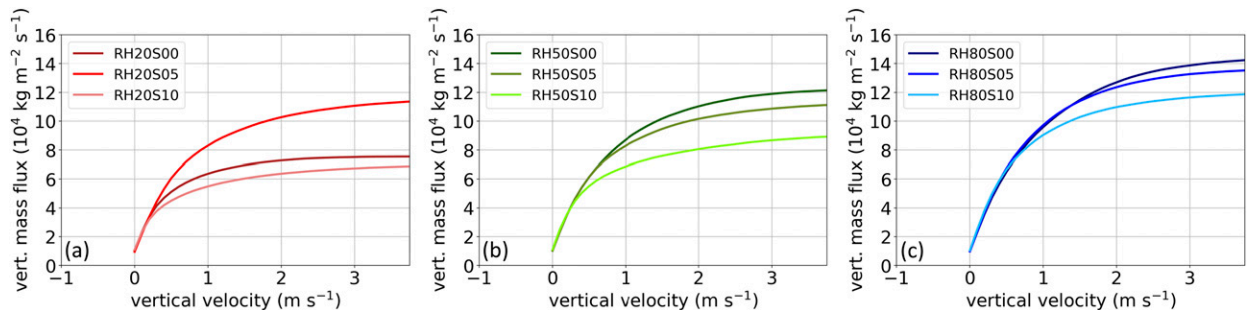

FIG. 6. Cumulative vertical mass flux ($\times 10^4$ kg m^{-2} s^{-1}) as a function of vertical velocity (m s^{-1}) for the (a) RH20, (b) RH50, and (c) RH80 experimental sets. The vertical mass flux is summed in a volume from the surface to a height of 1 km, and within 75 km of the TC center. Each panel is time averaged during the bifurcation time period.
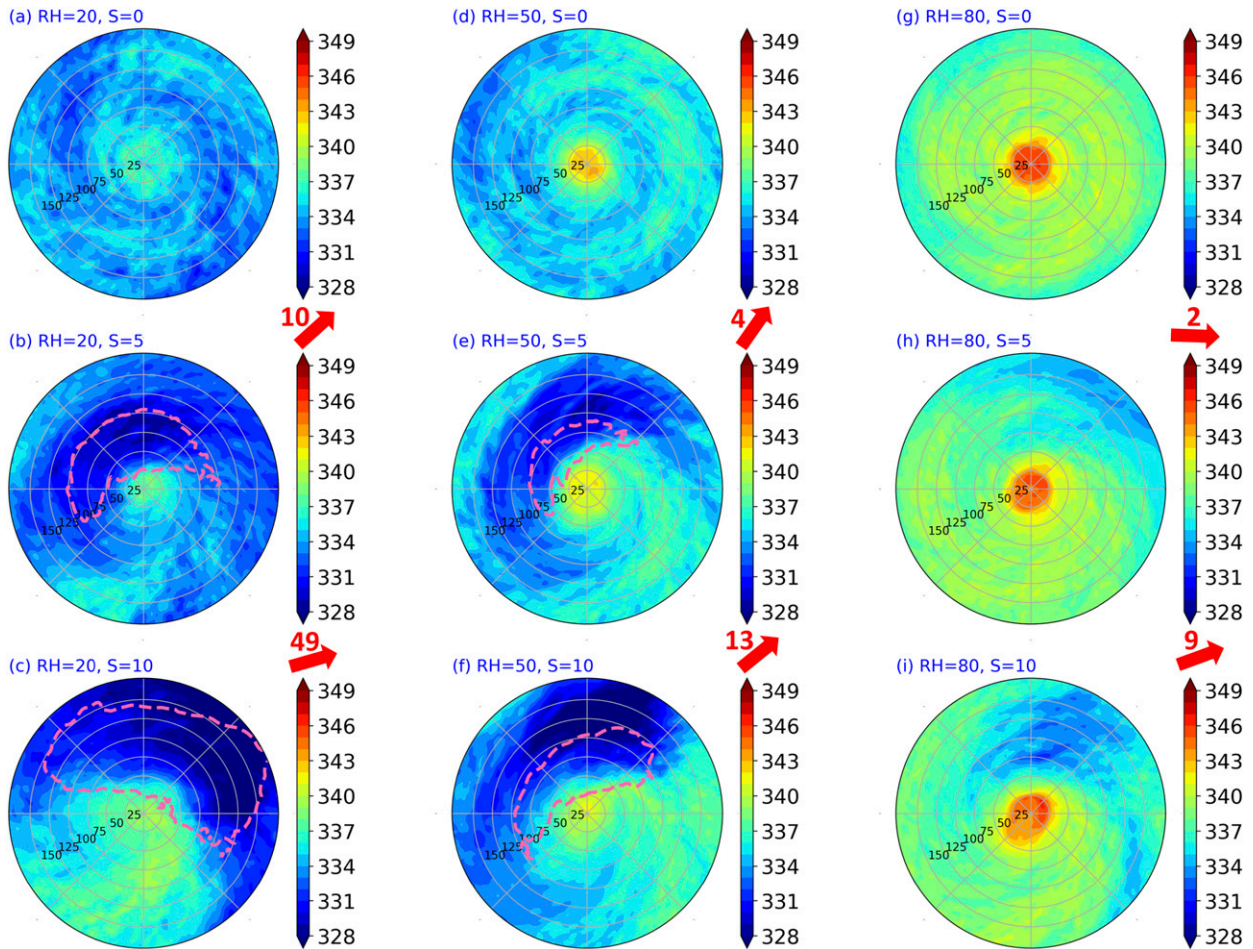
FIG. 7. Equivalent potential temperature (shaded, K) and buoyancy (magenta contour for a value of $-0.08\,\mathrm{m\,s^{-2}}$) averaged between heights of 0 and 1 km across the bivariate parameter space. Each panel is time averaged during the bifurcation time period. Buoyancy was calculated using the density potential temperature and a base state given by the initial sounding. Note that this base state was compared to a base state defined as the sum of azimuthal wavenumbers 0 and 1 of density potential temperature (Braun 2002; Smith et al. 2005; Foerster and Bell 2017), and both base states gave qualitatively similar spatial distributions. Recall that the VWS direction is westerly for all experiments.

occurs for vertical velocities greater than about $1\,\mathrm{m\,s^{-1}}$, as opposed to vertical velocities greater than $0.5\,\mathrm{m\,s^{-1}}$ in the RH20 experimental set. Since the total vertical mass fluxes are similar during the bifurcation time period for RH50S00 and RH50S05, the intensities (Fig. 2b) are similar between these two experiments.

The RH80 experimental set (Fig. 6c) has similar vertical mass flux magnitudes for vertical velocities less than about $1\,\mathrm{m\,s^{-1}}$. RH80S00 has more frequent vertical velocities greater than $1.5\,\mathrm{m\,s^{-1}}$, followed by RH80S05 and RH80S10, which supports RH80S00 being the strongest during this time period (Fig. 2c).

The key finding from Figs. 5 and 6 is that the areal extent of strong upward motions ($w > 0.5\,\mathrm{m\,s^{-1}}$) in the inner core controls the linear increase in vertical mass flux with TC intensity. This relationship is consistent with previous studies showing TC development being associated with an increased areal coverage of convection (Leppert et al. 2013a,b; Zawislak and Zipser 2014), especially when convection in sheared TCs encompasses the upshear-left quadrant (Stevenson et al. 2014; Rogers et al. 2015; Susca-Lopata et al. 2015; Rios-Berrios and Torn 2017; Fischer et al. 2018).

How does downdraft ventilation, and its effects on low-level θ_e, modulate the areal extent of strong upward motions and the vertical mass flux in the inner core, which is highly correlated with TC intensity? To answer this question, the next section explores the three-dimensional structure of downdraft ventilation, and the subsequent section assesses the impact of air from downdraft ventilation regions on convection in the inner core.

5. Downdraft ventilation

a. Horizontal structure of θ_e at low levels

To diagnose the spatial distribution of low-θ_e air in the subcloud layer, and to motivate the investigation of downdraft ventilation, Fig. 7 shows θ_e averaged between heights of 0 to 1 km during the bifurcation time period for each experiment. Differences arise in the structure of lower-θ_e air outside of the relatively higher-θ_e inner core. For the RH20 experimental set (Figs. 7a–c), RH20S00 has randomly distributed, lower-θ_e air
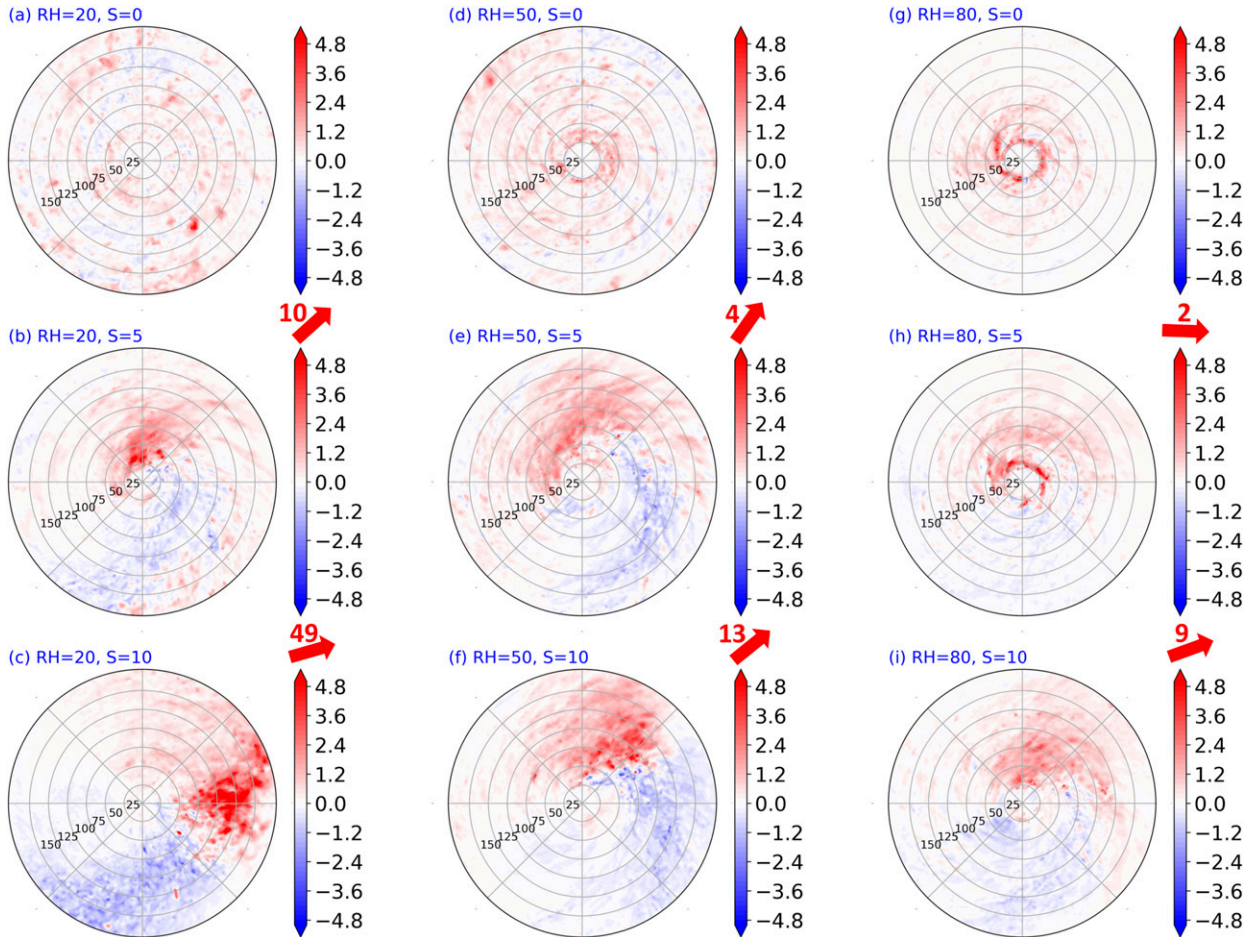
FIG. 8. Downdraft ventilation (kg K m^{-2} s^{-1}) at a height of 1 km across the bivariate parameter space. Only locations where the vertical velocity is less than zero are plotted. Red shading means downward motion of anomalously low-θ_e air. Each panel is time averaged during the bifurcation time period. Recall that the VWS direction is westerly for all experiments.

outside a radius of 40 km. RH20S05 has a region of lower-θ_e air, minimized left of shear outside the core, which wraps inward toward the TC center from the UL to the UR and DR quadrants. This region is within convection or cyclonically downwind (counterclockwise) of convection, in near-zero reflectivity (Fig. 4b). RH20S10 also has lower-θ_e air within and downstream of convection, but this air does not appear to wrap inward toward the circulation center, likely due to the weak circulation (Fig. 2a). For RH20S05 and RH20S10, the low-θ_e air left of shear is associated with negative buoyancy (<-0.08 m s^{-2}).

For the RH50 experimental set (Figs. 7d–f), both RH50S05 and RH50S10 have similar regions of lower-θ_e, negative-buoyancy air left of shear between radii of 60 and 150 km, although RH50S10 is associated with lower-θ_e air, which spirals radially inward in the DR quadrant. Similar to the RH20 experimental set, the region of lower-θ_e air is within, and downstream of, convection (Figs. 4e,f). The RH80 experimental set (Figs. 7g–i) shows a similar pattern, albeit with higher θ_e and buoyancy (no magenta contours). In the simulations with VWS, the region of lower-θ_e air looks similar to

that caused by downdraft ventilation associated with the quasi-stationary, azimuthal wavenumber-1 convective asymmetry discussed in Riemer et al. (2010). The differences in the horizontal distribution of θ_e in the subcloud layer for each experimental set suggest that low-θ_e, negative-buoyancy air is transported downward (i.e., downdraft ventilation exists) and inward toward the circulation center to potentially inhibit convection.

b. Horizontal structure of downdraft ventilation at a height of 1 km

Downdraft ventilation is defined as $\rho w' \theta_e'$, where ρ is density, and w is vertical velocity. Primes denote perturbations from the azimuthal mean. This term, when positive, represents the downward transport of relatively low-θ_e air into the subcloud layer, as discussed in Riemer et al. (2010). Downdraft ventilation is calculated at a height of 1 km, and only in locations where $w < 0$ are analyzed to focus on the *downward* transport of low-θ_e air into the subcloud layer.

The structure of downdraft ventilation varies for each experiment during the bifurcation time period (Fig. 8). No clear
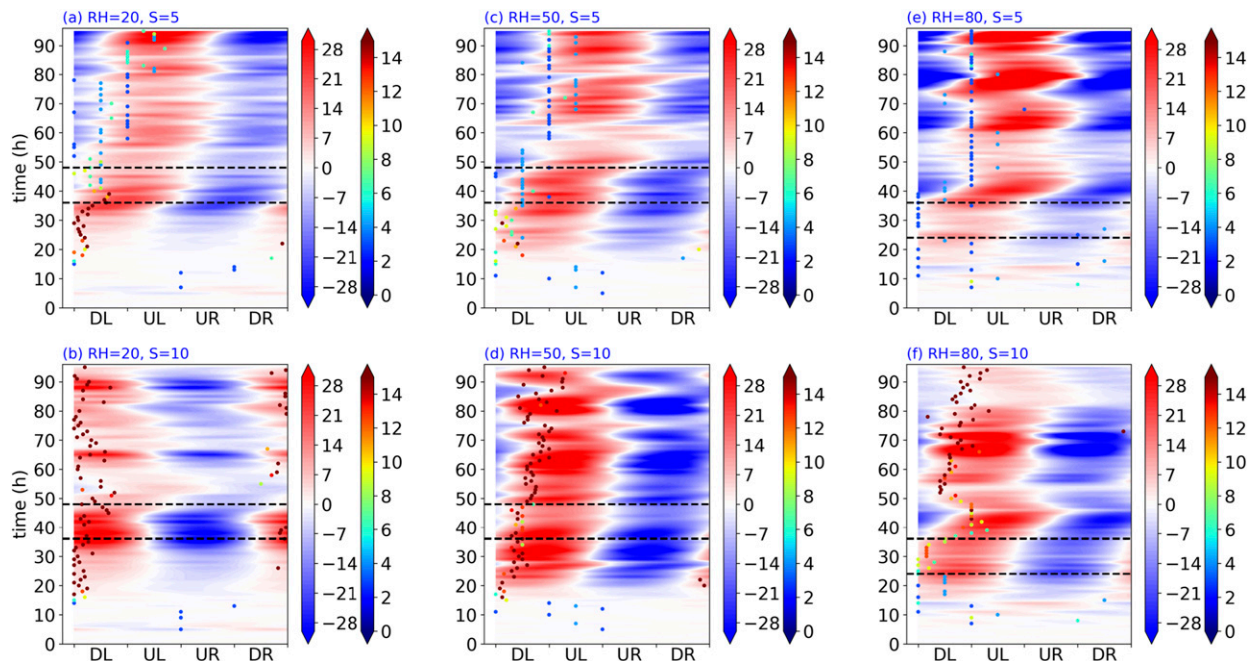
FIG. 9. Azimuth–time Hovmöller diagrams of the wavenumber-1 component of downdraft ventilation ($\times 10^{-2}$ kg K m^{-2} s^{-1}) at a height of 1 km in the bivariate parameter space. Downdraft ventilation has been radially averaged within the inner 150 km. Dots show the azimuthal direction of the vertical tilt from Fig. 3, and the color of each dot represents the magnitude of the vertical tilt. Dots are plotted every hour for vertical tilt magnitudes greater than 2 km. Black dashed horizontal lines show the beginning and end of the bifurcation time period for each experiment.

downdraft ventilation structure (red areas) exists outside a radius of 75 km for the S00 experiments (Figs. 8a,d,g), so we do not analyze these experiments hereafter. For the S05 and S10 experiments, downdraft ventilation occurs within, and downstream of, convection associated with rainbands (Fig. 4) and low-θ_e air (Fig. 7), consistent with the distribution of downdraft ventilation in previous literature (Riemer et al. 2010, 2013). For the RH20 experimental set (Figs. 8b,c), RH20S05 has downdraft ventilation left of shear, while RH20S10 has downdraft ventilation downshear. The RH50 (Figs. 8e,f) and RH80 (Figs. 8h,i) experimental sets have downdraft ventilation oriented left of shear. For each experimental set, the maximum magnitude of downdraft ventilation generally increases as the magnitude of the VWS increases, consistent with previous work connecting the downward transport of low-θ_e air to rainbands and the stationary band complex (Riemer et al. 2010, 2013; Riemer and Montgomery 2011).

The time evolution of the asymmetry of downdraft ventilation is explored next to determine what controls its structure. First, downdraft ventilation is examined by conducting an azimuthal Fourier decomposition of Fig. 8 and only keeping the wavenumber-1 component, as VWS primarily induces wavenumber-1 asymmetries (Jones 1995; Reasor et al. 2000; Corbosiero et al. 2006), and downdraft ventilation has a clear wavenumber-1 structure (Fig. 8). Figure 9 shows azimuth–time Hovmöller diagrams of the wavenumber-1 component of downdraft ventilation at a height of 1 km and averaged within the inner 150 km to capture the horizontal structure documented in Fig. 8. The magnitude and direction of the vertical tilt from

Fig. 3 is displayed as dots every hour if the tilt magnitude is greater than 2 km.

This analysis shows that the downdraft ventilation structure is associated with the vertical tilt of the vortex. For the RH20 experimental set (Figs. 9a,b), RH20S05 does not show a clear pattern during the first 24 h, during which time the VWS has not been fully implemented (Fig. 1c). After roughly 24 h, once the vertical tilt magnitude is greater than 15 km (Fig. 3a), a clear azimuthal asymmetry emerges, with downdraft ventilation extending cyclonically downstream through the left-of-shear semicircle. This asymmetry is consistent with the time-averaged downdraft ventilation in Fig. 8b. Importantly, downdraft ventilation is associated with, and downstream of, the vertical tilt direction. The vertical tilt is directed downshear with a magnitude greater than 14 km at 30 h. From 30 to 50 h, the vertical tilt rotates cyclonically to the DL quadrant and decreases in magnitude, potentially associated with vortex precession (Zhang and Tao 2013). Downdraft ventilation rotates cyclonically with the vertical tilt direction, and weakens slightly as the tilt magnitude decreases around 40 h. RH20S10 shows a similar pattern, with downdraft ventilation associated with, and downstream of, the vertical tilt direction. The vertical tilt is directed downshear with a magnitude greater than 14 km throughout this experiment. This consistent tilt direction is associated with a consistent azimuthal asymmetry of downdraft ventilation extending from the DR to UL quadrants.

The RH50 (Figs. 9c,d) and RH80 (Figs. 9e,f) experimental sets show a similar pattern between the azimuthal asymmetry of downdraft ventilation and the vertical tilt direction. The
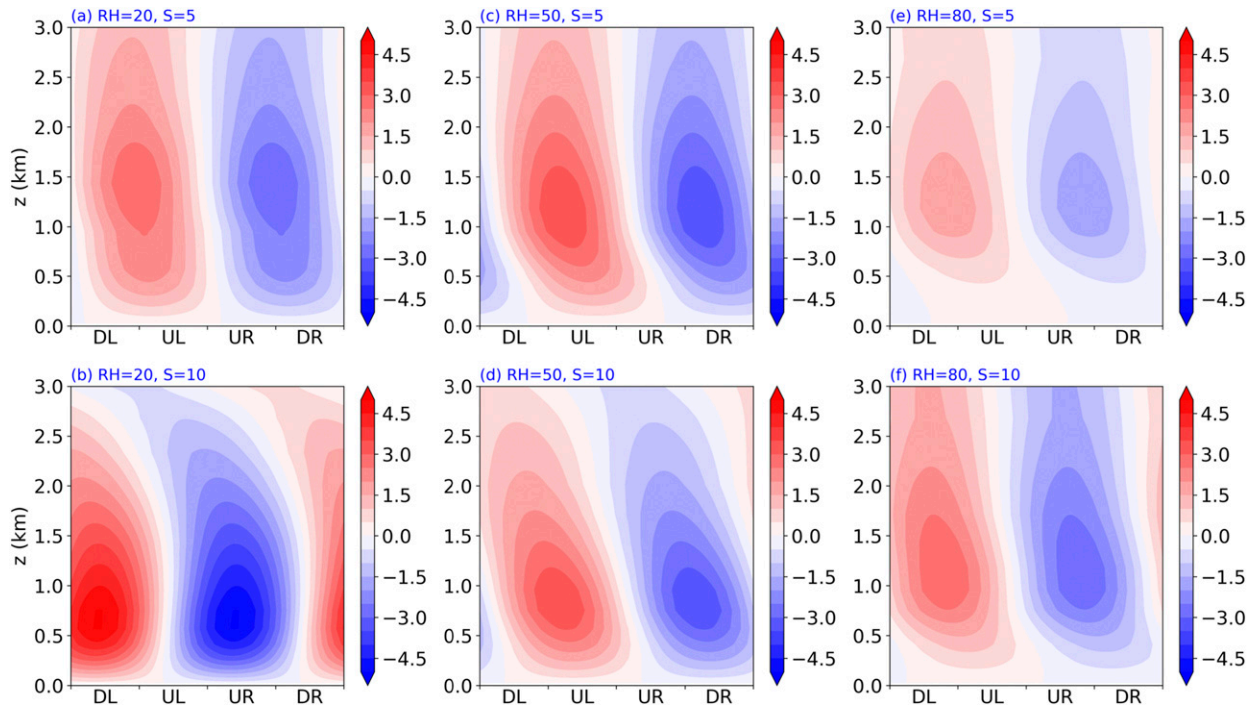
FIG. 10. Azimuth–height diagrams of the wavenumber-1 component of downdraft ventilation ($\times 10^{-1}$ kg K m^{-2} s^{-1}) in the bivariate parameter space. Downdraft ventilation has been radially averaged within the inner 150 km and time averaged during the bifurcation time period.

relationship is most clearly visualized in RH80S10, in which both the azimuthal asymmetry of downdraft ventilation and the vertical tilt direction rotate cyclonically between 30 and 45 h. This consistent pattern suggests that downdraft ventilation is located cyclonically downstream from the vertical tilt direction. These results agree with previous literature that associates the rainband structure with the vertical tilt of the vortex (Riemer 2016), and provides new evidence that the azimuthal asymmetry of downdraft ventilation is tied to the vertical tilt, as also shown, but not explicitly mentioned, in Riemer et al. (2010) and Tao and Zhang (2014).

c. Vertical structure of downdraft ventilation

The previous section concentrated on the horizontal structure of downdraft ventilation at a height of 1 km, but what is its vertical structure? Specifically, at what height is downdraft ventilation maximized, and how far does downdraft ventilation extend to the surface? Downdraft ventilation that extends closer to the surface may be more detrimental on TC development. Figure 10 presents azimuth–height diagrams of the wavenumber-1 component of downdraft ventilation from the surface to a height of 3 km. The wavenumber-1 component is analyzed because downdraft ventilation has a clear wavenumber-1 structure at each height from the surface to 3 km. Downdraft ventilation has been radially averaged within the inner 150 km and time averaged during the bifurcation time period.

For the RH20 experimental set (Figs. 10a,b), RH20S05 has downdraft ventilation left of shear, consistent with Fig. 8b,

maximized at a height of 1.5 km, and extending downward to 0.1 km. For RH20S10, downdraft ventilation is stronger, maximized at a lower height of 0.75 km, and extends closer to the surface compared to RH20S05. These results suggest that downdraft ventilation in RH20S10, with lower-θ_e air, penetrates lower down in the subcloud layer compared to RH20S05. This result is explored further using trajectories in section 6.

For the RH50 experimental set (Figs. 10c,d), RH50S05 has downdraft ventilation maximized at a height of 1.1 km that extends downward to 0.1 km, similar to RH20S05. Unlike RH20S05, the azimuthal asymmetry in RH50S05 rotates cyclonically when extending downward from 1.1 to 0.1 km, which is associated with a cyclonically rotating vertical tilt structure (not shown). For RH50S10, downdraft ventilation is maximized at a height of 0.75 km, a lower vertical level compared to RH50S05, but also rotates cyclonically when moving downward toward the surface.

For the RH80 experimental set (Figs. 10e,f), downdraft ventilation is generally weaker than the RH20 and RH50 experimental sets. RH80S05 has downdraft ventilation maximized at a height of roughly 1.3 km that only extends downward to a height of roughly 0.5 km. RH80S10 has downdraft ventilation maximized at about the same height of 1.3 km and extends downward to about 0.25 km.

The vertical structure of downdraft ventilation suggests that weaker TCs embedded in drier and higher VWS environments (and having larger vertical tilts) have a stronger downward transport of low-θ_e air penetrating lower down toward the surface. It remains to be shown, however, if this low-θ_e air gets
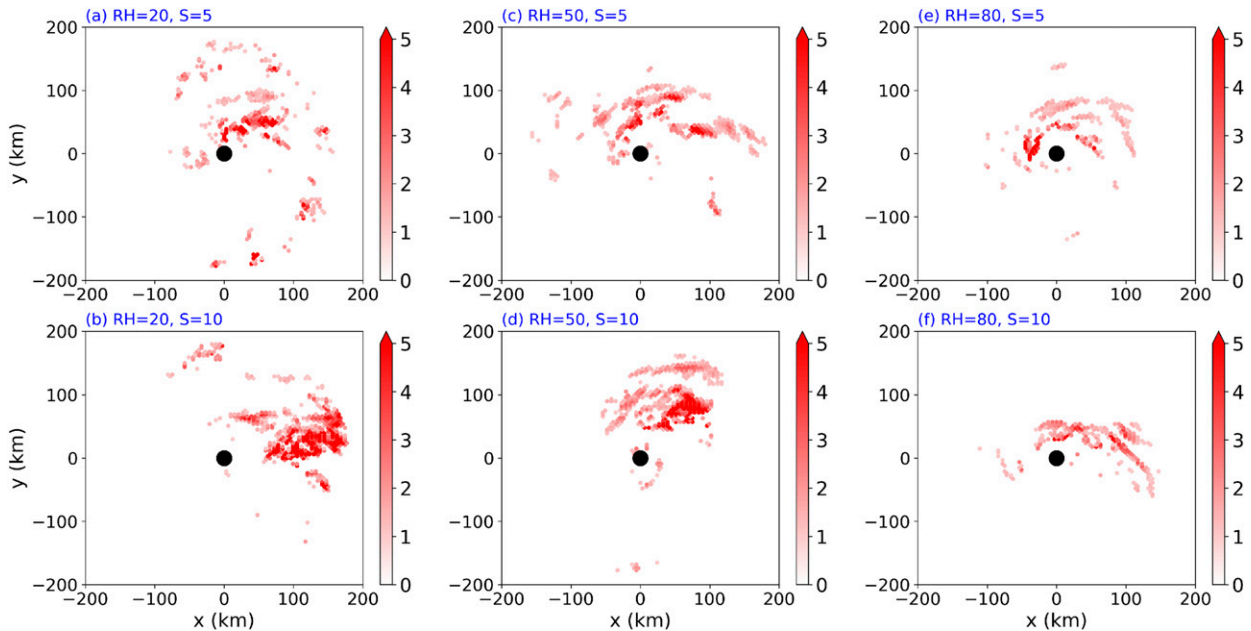
FIG. 11. Trajectory initialization locations (red dots) in downdraft ventilation (kg K m^{-2} s^{-1}) for the S05 and S10 experiments in the bivariate parameter space. Trajectories were initialized at the beginning of each bifurcation time period, at a height of 1 km, within the inner 180 km, and for an initial downdraft ventilation magnitude of at least 1 kg K m^{-2} s^{-1}. Every two trajectory initialization locations are plotted. The black dot in each panel represents the center of the TC at the lowest model level.

transported radially in the inflow layer toward the inner core. If so, how does this low-θ_e air affect the distribution and strength of convection? Previous literature investigating mature TCs has shown that if surface fluxes do not recover the θ_e, convection weakens (Riemer et al. 2010). The next section utilizes trajectories to investigate if downdraft ventilation frustrates upward motions in the weak TCs, or if surface fluxes are able to recover the θ_e of this air before ascending in the inner core.

6. Effects of downdraft ventilation on convection: Trajectory analysis

We use the Lagrangian Analysis Tool (Lagranto) to compute forward trajectories (Wernli and Davies 1997; Sprenger and Wernli 2015). Trajectories were calculated using 6-min model output files that were then interpolated to a 1-min

frequency. Trajectories were initialized in downdraft ventilation regions and integrated forward for 24 h to analyze parcel movements, thermodynamic evolutions, and effects of this air on convection in the inner core. Note that backward trajectories were also conducted from strong upward motions in the inner core, and the vast majority of trajectories originated in downdraft ventilation regions. Since no clear ventilation structure was found for the S00 experiments (Figs. 8a,d,g), Fig. 11 shows the initialization locations of the trajectories only for the S05 and S10 experiments. Each trajectory is initialized at the beginning of the bifurcation time period, at a height of 1 km, and within the inner 180 km to fully capture the downdraft ventilation structures in Fig. 8. Trajectories were initialized for an initial downdraft ventilation magnitude of at least 1 kg K m^{-2} s^{-1} to focus on the strongest downdraft ventilation regions, and Table 2 lists the number of trajectories initialized for each experiment. The online

TABLE 2. Number of trajectories initialized in downdraft ventilation regions in the inner 180 km and at a height of 1 km, the fraction of those trajectories rising above 5 km within the inner core, and the average θ_e of trajectories in the DR inner core below 1 km, for the S05 and S10 experiments. Initialization occurs at the beginning of the bifurcation time period for each experiment and trajectories were integrated forward for 24 h with output every minute.

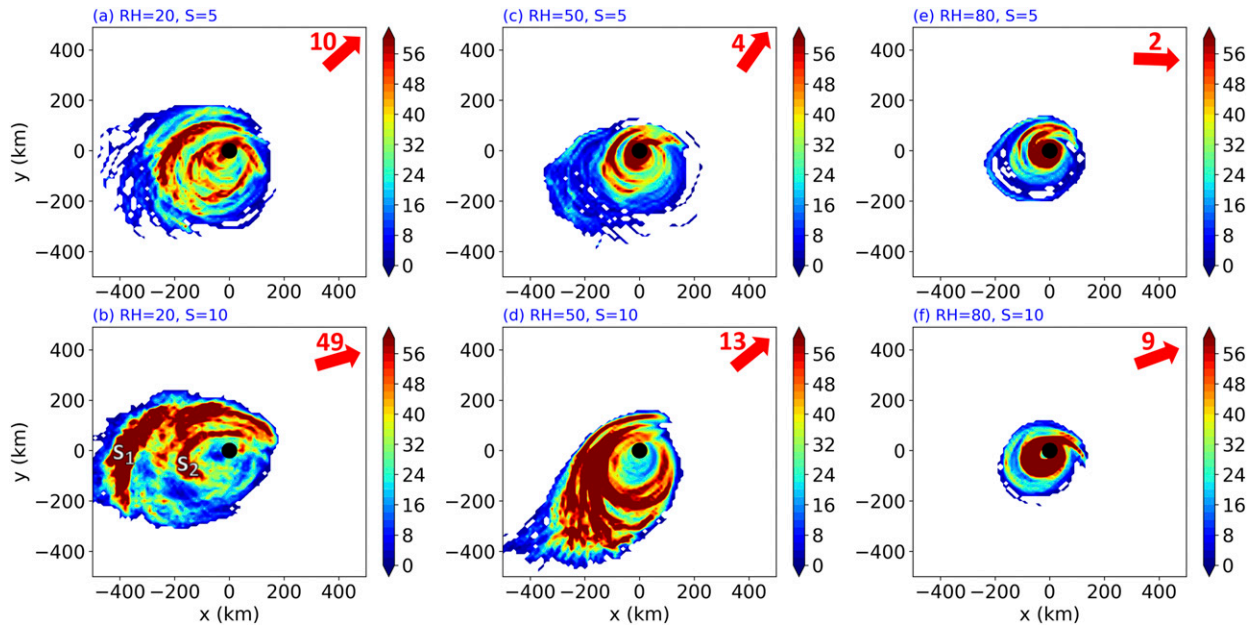| Experiment	Number of trajectories	Fraction rising above 5 km (%)	Average θ_e (K)
RH20S05	709	41	336.5
RH20S10	973	7	339.3
RH50S05	815	70	337.6
RH50S10	873	16	340.1
RH80S05	501	86	340.7
RH80S10	473	77	341.6

FIG. 12. Number of downdraft ventilation trajectories passing through a location ($\times 10^{-2}$) during the 24-h integration across the bivariate parameter space. The number has been normalized by the total number of trajectories initialized listed in Table 2. Only parcels below a height of 1 km are presented to focus on parcel movement in the subcloud layer. The vertical tilt magnitude (km) and direction between the surface and a height of 6 km, time averaged during the bifurcation time period, are represented by the red number and arrow, respectively, at the top right of each panel.

supplement contains animations of the parcels comprising the trajectories for each set.

Figure 12 shows the normalized trajectory density during the 24-h integration. Note that only parcel locations below 1 km are

shown in these panels to focus on parcel movement within the subcloud layer. Trajectory streams are defined as maxima in trajectory density. For the RH20 experimental set (Figs. 12a,b), RH20S05 has parcels that rotate cyclonically around the TC
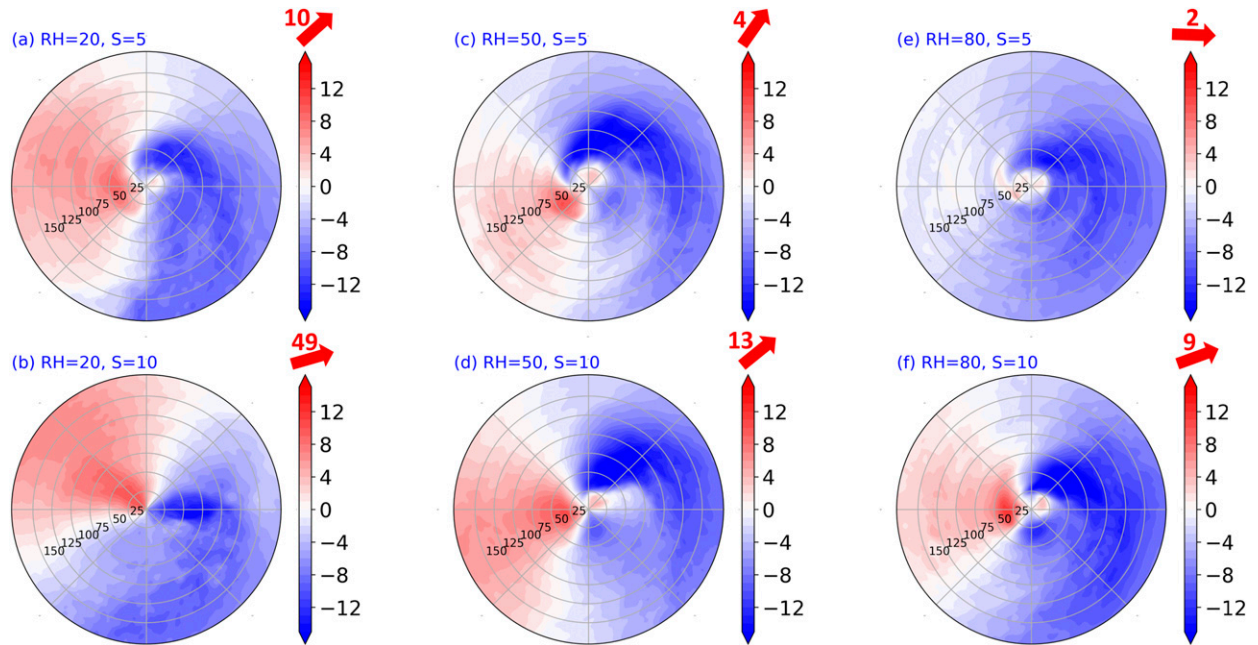

FIG. 13. Radial velocity (m s^{-1}) averaged between heights of 0 and 1 km. Positive values signify radial outflow and negative values signify radial inflow. Each panel is time averaged during the bifurcation time period.
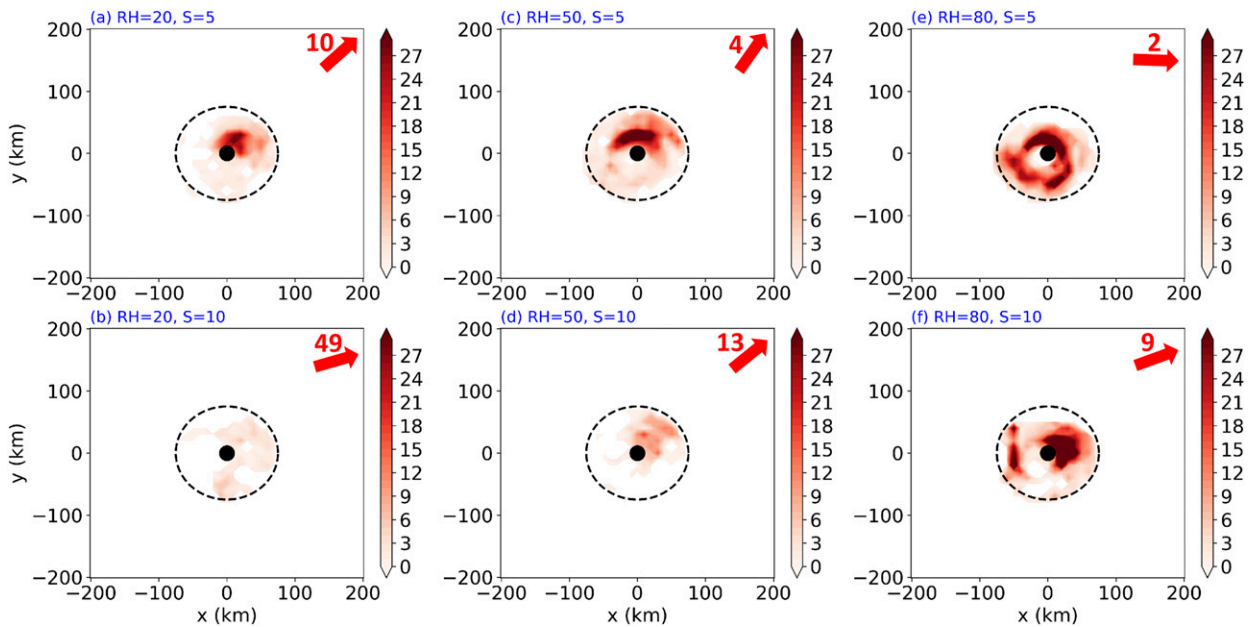
FIG. 14. Number of downdraft ventilation trajectories ($\times 10^{-2}$), below a height of 2 km, with a vertical velocity greater than $0.5\,\mathrm{m\,s^{-1}}$ in the inner core during the 24-h integration across the bivariate parameter space. The number has been normalized by the total number of trajectories initialized listed in Table 2. The dashed circle represents the inner 75 km.

center from their initial locations in Fig. 11a. Parcels move radially outward in the UL quadrant and radially inward in the DR quadrant (Fig. 13a). This radial flow pattern is consistent with previous literature on sheared TCs (DeHart et al. 2014). Multiple streams of trajectories exist. All streams move radially outward in the UL quadrant, but parcels in the first stream rotate around the TC faster and reach the DR quadrant sooner, upon which these parcels are transported radially inward. The parcels are then transported close to the TC center downshear. Most of

the parcels rise downshear and in the DL quadrant, as illustrated by Fig. 14a, which shows the normalized trajectory density of strong upward motions in the inner core.

RH20S10 has trajectories that are initialized more downshear and radially outward compared to trajectories in RH20S05 (Fig. 11b). Similar to RH20S05, however, parcels move to the UL quadrant and are transported radially outward (Figs. 12b and 13b). Two streams of trajectories exist (s_1 and s_2), and these streams extend outward to larger radii compared to
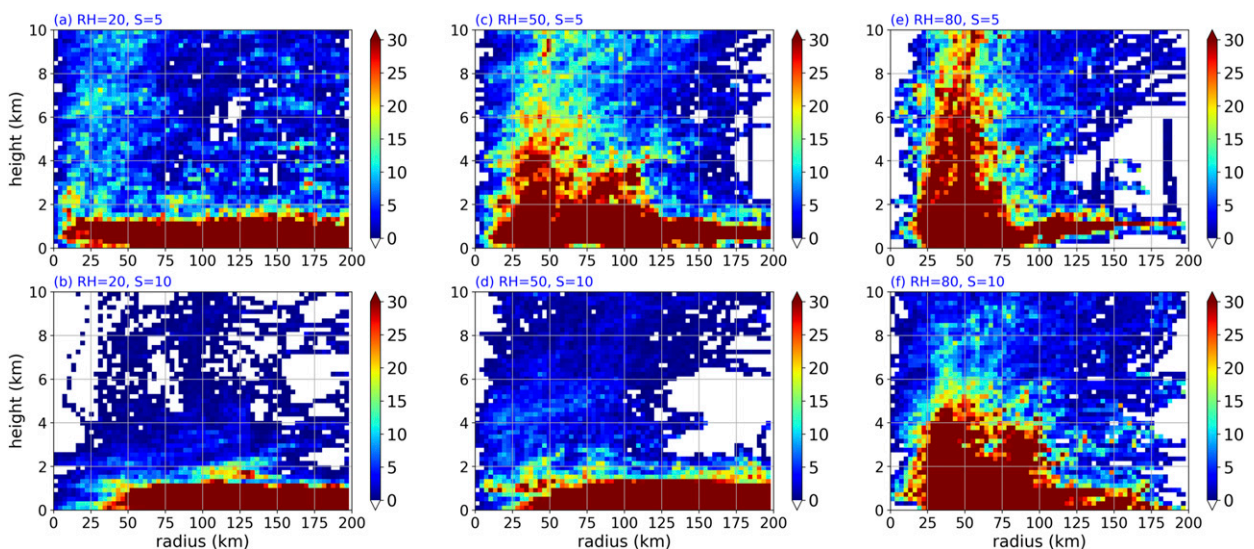

FIG. 15. Radius–height diagrams of the number of downdraft ventilation trajectories passing through a location ($\times 10^{-2}$) during the 24-h integration. The number has been normalized by the total number of trajectories initialized listed in Table 2.
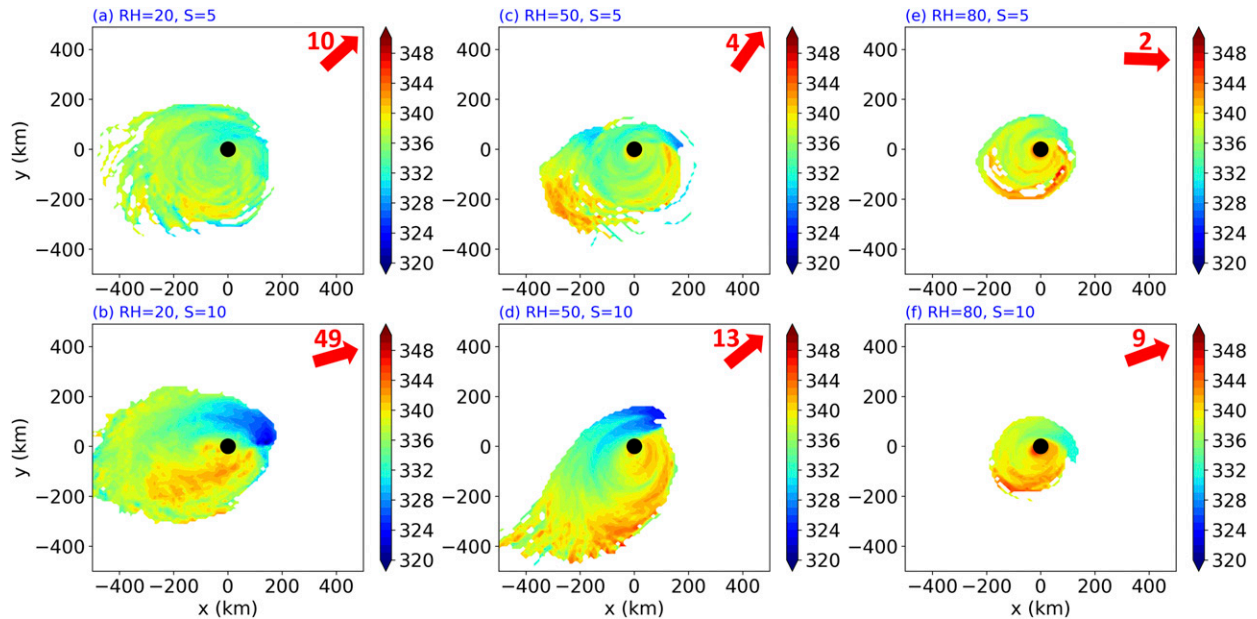
FIG. 16. As in Fig. 12, but for the average equivalent potential temperature (K). Note that the same trajectories as in Fig. 12 were used here.

RH20S05, due to a larger vertical tilt (red arrows) in RH20S10 and stronger low-level radial outflow (Fig. 13b), associated with the dynamic response of a tilted vortex (DeHart et al. 2014). The outflow upshear decreases the net inward transport to the inner core, effectively reducing upward motions in this region, with only a few parcels reaching downshear and rising (Fig. 14b).

The RH50 experimental set (Figs. 12c,d) shows a similar pattern as RH20S10, with two streams of trajectories. RH50S05 has parcels rotating closer to the TC center compared to the RH20 experiments due to a smaller vertical tilt and reduced radial outflow in the UL quadrant (Fig. 13c). RH50S10 consists of trajectory streams farther from the TC center than RH50S05 due to greater radial outflow in the upshear semicircle (Fig. 13d). The trajectories form a similar inward-directed corridor in the DR quadrant, but the majority of parcels do not rise until reaching the DL quadrant (Fig. 14d).

For RH80S05 (Fig. 12e), the majority of trajectories remain within the inner 100 km, while rotating cyclonically about the TC center, with parcels rising about all azimuths (Fig. 14e). RH80S10 (Fig. 12f) shows a similar pattern as RH80S05, albeit with parcels displaced more radially outward upshear and rising motion concentrated downshear (Fig. 14f).

To compare the number of trajectories that rise in each experiment, Fig. 15 shows radius–height diagrams of the trajectory density during the 24-h integration. For all experiments, most of the parcels stay below a height of 2 km, with the S05 experiments having more parcels rising in the inner core compared to their S10 counterparts. Table 2 quantifies this result by listing the percentage of trajectories that rise above 5 km during the 24-h integration. For the RH20 experimental set, 41% of RH20S05 trajectories rise above 5 km, but only 7% rise above 5 km for RH20S10. The RH50 experimental set shows a similar pattern: 70% of trajectories rise above 5 km for RH50S05, but only 16% rise above 5 km for RH50S10. The

RH80 experimental set has the majority of trajectories rising above 5 km for both experiments (86% and 77% for RH80S05 and RH80S10, respectively) in association with smaller vertical tilts (Figs. 12e,f) and larger areas of strong upward motions (Figs. 5 and 6c) compared to the other experimental sets.

To determine if trajectories from downdraft ventilation regions reach the inner core with low θ_e to potentially inhibit convection, Fig. 16 shows the average θ_e of trajectories below a height of 1 km during the 24-h integration, and Table 2 lists the average θ_e of trajectories in the DR inner core. For the RH20 experimental set (Figs. 16a,b), RH20S05 has parcels that start with a higher initial θ_e compared to RH20S10. As parcels rotate cyclonically for both experiments, surface fluxes increase the θ_e of most parcels. The increase is particularly noticeable when parcels are in the inflow corridor right of shear and in the DR quadrant. RH20S10 has parcels that appear to recover faster, associated with a larger air–sea disequilibrium (not shown), to a higher θ_e in the DR inner core of 339.3 K, compared to 336.5 K for RH20S05 (difference of 2.8 K). For RH20S10, even parcels 300 km southwest of the center have θ_e values around 340 K.

The RH50 (Figs. 16c,d) and RH80 (Figs. 16e,f) experimental sets show low-θ_e trajectories associated with downdraft ventilation quickly recover in the subcloud layer from surface fluxes. RH50S10 and RH80S10 have increased θ_e values of roughly 2.5 and 1 K compared to their S05 counterpart, respectively (Table 2), in the DR inner core (Figs. 16d,f). This recovery demonstrates that parcels originating in downdraft ventilation regions that enter the inner core can have high θ_e and feed convection downshear. Although the parcels recover before rising, the experiments with higher magnitudes of VWS have a smaller percentage of parcels rising above 5 km (Fig. 15), associated with a smaller areal extent of strong upward motions (Figs. 5 and 6). The downward transport of low-θ_e, negative-buoyancy

air from downdraft ventilation regions, along with low-level radial outflow upshear (Fig. 13), aid in reducing the areal extent of strong upward motions left of shear and in the upshear semicircle, thereby reducing the vertical mass flux in the inner core, and stunting TC development (Fig. 2).

7. Conclusions

This study discussed the modulating effects of downdraft ventilation on the vertical mass flux in the TC inner core and TC development. A strong, positive, linear relationship existed between the low-level vertical mass flux in the inner core and TC intensity, with a larger vertical mass flux associated with a stronger intensity. The linear increase in vertical mass flux with intensity was not due to an increased *strength* of upward motions but, instead, was due to an increased *areal extent* of strong upward motions ($w > 0.5 \, \mathrm{m \, s^{-1}}$). This relationship suggests physical processes that could influence the vertical mass flux, such as downdraft ventilation, influence the intensity of a TC.

The three-dimensional structure of downdraft ventilation across the moisture–VWS parameter space was diagnosed. No clear structure existed for the experiments without VWS (S00). For the experiments with VWS (S05 and S10), downdraft ventilation occurred within and downstream of convection associated with rainbands, consistent with previous literature (Riemer et al. 2010). The azimuthal asymmetry and strength of downdraft ventilation was found to be associated with the vertical tilt of the vortex: downdraft ventilation was cyclonically downstream from the vertical tilt direction and its strength was associated with the magnitude of the vertical tilt. These results agree with previous literature that associates the principal rainband location with the vertical tilt (Riemer 2016) and provides new understanding of the relationship between the azimuthal asymmetry of downdraft ventilation and the vertical tilt. The vertical structure of downdraft ventilation suggests that weaker TCs embedded in drier and higher VWS environments (and having larger vertical tilts) are generally associated with stronger downdraft ventilation extending lower down toward the surface.

This study also utilized trajectories to study the pathways by which low-θ_e, negative-buoyancy air associated with downdraft ventilation was transported into the inner core at low levels and its effects on convection for weak TCs. Low-θ_e parcels associated with downdraft ventilation trajectories recovered via surface fluxes in the subcloud layer. The S10 experiments had θ_e values that recovered faster and reached a higher magnitude when approaching the inner core in the DR quadrant compared to their S05 counterparts. Importantly, this recovery demonstrates that parcels originating in downdraft ventilation regions that enter the inner core can have high θ_e that does not inhibit convection downshear. Instead, the inhibiting effects were the downward transport of low-θ_e, negative-buoyancy air from downdraft ventilation regions, and the associated low-level radial outflow upshear, which reduced the areal extent of strong upward motions left of shear and in the upshear semicircle, decreasing the vertical mass flux in the inner core, and stunting TC development. These inhibitive effects were stronger for TCs embedded in drier and higher VWS environments. The results presented in this study complement previous literature that discusses the spatial structure of downdraft ventilation (Riemer et al. 2010, 2013) and the radial flow structure associated with sheared TCs (e.g., DeHart et al. 2014), and add to existing knowledge by demonstrating the connection of downdraft ventilation in weak TCs with the areal extent of strong upward motions, which is shown here to be strongly associated with TC intensity.

A conceptual model of how downdraft ventilation modulates TC development is shown in Fig. 17 for a representative
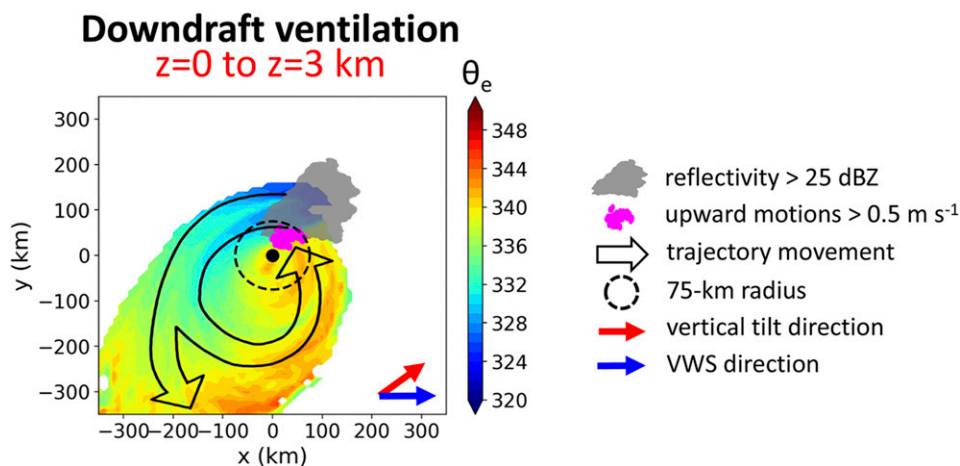

FIG. 17. Conceptual model of downdraft ventilation based on the RH50S10 experiment showing the average equivalent potential temperature of trajectories initialized in downdraft ventilation regions (K, colored shading), reflectivity greater than 25 dBZ (gray shading), upward motion greater than $0.5 \, \mathrm{m \, s^{-1}}$ (magenta dots), parcel movement (black arrows), the inner 75 km (dashed circle), the vertical tilt direction from the surface to 6 km (red arrow), and the VWS direction (blue arrow). The reflectivity and vertical velocity are time averaged during the bifurcation time period.

experiment, RH50S10. Trajectories initialized in downdraft ventilation regions, coinciding with convection (gray shading) and cyclonically downstream from the vertical tilt direction, are associated with low-θ_e air (colored shading). These parcels are transported cyclonically and radially outward in the upshear semicircle, due to radial outflow at low levels. One stream of trajectories, initialized closer to the TC center, is transported radially inward in the DR quadrant into the inner core. A second stream of trajectories, initialized farther from the TC center compared to the first stream, continues to move radially outward in the UR quadrant. Both streams are associated with an increase in θ_e, due to surface fluxes, as the parcels rotate cyclonically. Parcels that enter the inner core in the DR quadrant and downshear, associated with recovered θ_e, rise in strong upward motions (magenta dots).

This study showed a strong, positive, linear relationship between the low-level vertical mass flux in the inner 75 km and TC intensity. Future work should examine if this linear relationship holds in other modeling frameworks and observational analyses. In addition, a theoretical underpinning behind the linear relationship is needed, specifically why this linear relationship exists for a certain radius (i.e., 75 km in this study), that takes into account internal and environmental parameters that may be relevant to this relationship.

Downdraft ventilation was the focus of this study, but what is the three-dimensional structure of radial ventilation? Additionally, how does radial ventilation affect inner-core convection? Does dry air get into upward motions to decrease the θ_e and reduce the strength of convection, as suggested in previous literature (Tang and Emanuel 2010)? Part II focuses on these questions.

APPENDIX

Large-Scale Wind Acceleration and Nudging

In these simulations, the governing equations for horizontal velocity ($u_i = u, v$) include a prescribed acceleration term that is a function of height only: $(\partial u_i / \partial t) = \cdots + P_i(z)$. Such a term has been used in small-scale modeling of atmospheric flow for a long time (e.g., Sommeria 1976) to crudely approximate a

large-scale pressure gradient and to avoid complicated three-dimensional balanced initial conditions. We use the geostrophic equation to determine the magnitude of these terms: $P_1(z) = -f v_g$ and $P_2(z) = f u_g$, where $u_g(z)$ and $v_g(z)$ are prescribed geostrophic velocity profiles. For simplicity, we set u_g and v_g equal to the initial wind profiles at $t = 0$. As in many other studies that use this technique (e.g., Moeng 1984; Skamarock et al. 1994; Davis and Weisman 1994; Nolan and Rappin 2008; Nolan 2011; Zhang and Tao 2013), a large-scale horizontal temperature gradient that would be needed to satisfy thermal-wind balance is not included in the simulations. This choice is made for simplicity, and presumably because the effects of large-scale temperature variations are negligible on short-duration simulations.

All simulations begin with no mean flow, which facilitates the development of convection in the TC inner core. After 12 h, mean flow with vertical wind shear is gradually added to the simulation via nudging terms:

$$\frac{\partial u}{\partial t} = \cdots - \frac{\langle u \rangle - u_r}{\tau_n}, \quad \text{(A1a)}$$

$$\frac{\partial v}{\partial t} = \cdots - \frac{\langle v \rangle - v_r}{\tau_n}, \quad \text{(A1b)}$$

where brackets represents a horizontal average (on constant height levels) over the entire domain that are recomputed every time step; $u_r(z,t)$ and $v_r(z,t)$ are reference wind profiles that the flow is nudged toward; and τ_n is a relaxation time scale. The goal of this formulation is to gradually nudge the *domain-average* winds to desired profiles. This technique is similar to the "time-varying point-downscaling" technique of Onderlinde and Nolan (2017), except their approach acts to nudge every wind profile in the domain independently toward a reference profile, whereas our method only modifies the domain-average wind profiles [because the terms on the right side of (A1) are functions of height only]. An advantage of our method is that it does not directly add vertical vorticity to the simulation via the nudging terms. When (A1) is included, the geostrophic wind profiles used in the P_i terms are modified consistently:

$$\frac{\partial u_g}{\partial t} = -\frac{u_g - u_r}{\tau_n}, \quad \text{(A2a)}$$

$$\frac{\partial v_g}{\partial t} = -\frac{v_g - v_r}{\tau_n}. \quad \text{(A2b)}$$

REFERENCES

Alland, J. J., B. H. Tang, and K. L. Corbosiero, 2017: Effects of midlevel dry air on development of the axisymmetric tropical cyclone secondary circulation. *J. Atmos. Sci.*, **74**, 1455–1470, https://doi.org/10.1175/JAS-D-16-0271.1.

——, ——, ——, and G. H. Bryan, 2021: Combined effects of midlevel dry air and vertical wind shear on tropical cyclone development. Part II: Radial ventilation. *J. Atmos. Sci.*, **78**, 783–796, https://doi.org/10.1175/JAS-D-20-0055.1.

Barnes, G. M., E. J. Zipser, D. Jorgensen, and F. Marks Jr., 1983: Mesoscale and convective structure of a hurricane rainband. *J. Atmos. Sci.*, **40**, 2125–2137, https://doi.org/10.1175/1520-0469(1983)040<2125:MACSOA>2.0.CO;2.

Bracken, W. E., and L. F. Bosart, 2000: The role of synoptic-scale flow during tropical cyclogenesis over the North Atlantic Ocean. *Mon. Wea. Rev.*, **128**, 353–376, https://doi.org/10.1175/1520-0493(2000)128<0353:TROSSF>2.0.CO;2.

Braun, S. A., 2002: A cloud-resolving simulation of Hurricane Bob (1991): Storm structure and eyewall buoyancy. *Mon. Wea. Rev.*, **130**, 1573–1592, https://doi.org/10.1175/1520-0493(2002)130<1573:ACRSOH>2.0.CO;2.

——, J. A. Sippel, and D. S. Nolan, 2012: The impact of dry mid-level air on hurricane intensity in idealized simulations with no mean flow. *J. Atmos. Sci.*, **69**, 236–257, https://doi.org/10.1175/JAS-D-10-05007.1.

Bryan, G. H., 2012: Effects of surface exchange coefficients and turbulence length scales on the intensity and structure of numerically simulated hurricanes. *Mon. Wea. Rev.*, **140**, 1125–1143, https://doi.org/10.1175/MWR-D-11-00231.1.

——, and J. M. Fritsch, 2002: A benchmark simulation for moist nonhydrostatic numerical models. *Mon. Wea. Rev.*, **130**, 2917–2928, https://doi.org/10.1175/1520-0493(2002)130<2917:ABSFMN>2.0.CO;2.

——, and R. Rotunno, 2009: The maximum intensity of tropical cyclones in axisymmetric numerical model simulations. *Mon. Wea. Rev.*, **137**, 1770–1789, https://doi.org/10.1175/2008MWR2709.1.

——, and H. Morrison, 2012: Sensitivity of a simulated squall line to horizontal resolution and parameterization of microphysics. *Mon. Wea. Rev.*, **140**, 202–225, https://doi.org/10.1175/MWR-D-11-00046.1.

Chen, S. S., J. A. Knaff, and F. D. Marks, 2006: Effects of vertical wind shear and storm motion on tropical cyclone rainfall asymmetries deduced from TRMM. *Mon. Wea. Rev.*, **134**, 3190–3208, https://doi.org/10.1175/MWR3245.1.

Computational and Information Systems Laboratory, 2017: Cheyenne: HPE/SGI ICE XA System (Climate Simulation Laboratory). National Center for Atmospheric Research, https://doi.org/10.5065/D6RX99HX.

Corbosiero, K. L., and J. Molinari, 2002: The effects of vertical wind shear on the distribution of convection in tropical cyclones. *Mon. Wea. Rev.*, **130**, 2110–2123, https://doi.org/10.1175/1520-0493(2002)130<2110:TEOVWS>2.0.CO;2.

——, ——, A. R. Aiyyer, and M. L. Black, 2006: The structure and evolution of Hurricane Elena (1985). Part II: Convective asymmetries and evidence for vortex Rossby waves. *Mon. Wea. Rev.*, **134**, 3073–3091, https://doi.org/10.1175/MWR3250.1.

Cram, T. A., J. Persing, M. T. Montgomery, and S. A. Braun, 2007: A Lagrangian trajectory view on transport and mixing processes between the eye, eyewall, and environment using a high-resolution simulation of Hurricane Bonnie (1998). *J. Atmos. Sci.*, **64**, 1835–1856, https://doi.org/10.1175/JAS3921.1.

Davis, C. A., and M. L. Weisman, 1994: Balanced dynamics of mesoscale vortices produced in simulated convective systems. *J. Atmos. Sci.*, **51**, 2005–2030, https://doi.org/10.1175/1520-0469(1994)051<2005:BDOMVP>2.0.CO;2.

DeHart, J. C., R. A. Houze, and R. F. Rogers, 2014: Quadrant distribution of tropical cyclone inner-core kinematics in relation to environmental shear. *J. Atmos. Sci.*, **71**, 2713–2732, https://doi.org/10.1175/JAS-D-13-0298.1.

DeMaria, M., 1996: The effect of vertical shear on tropical cyclone intensity change. *J. Atmos. Sci.*, **53**, 2076–2088, https://doi.org/10.1175/1520-0469(1996)053<2076:TEOVSO>2.0.CO;2.

——, and J. Kaplan, 1994: A Statistical Hurricane Intensity Prediction Scheme (SHIPS) for the Atlantic basin. *Wea. Forecasting*, **9**, 209–220, https://doi.org/10.1175/1520-0434(1994)009<0209:ASHIPS>2.0.CO;2.

——, M. Mainelli, L. K. Shay, J. A. Knaff, and J. Kaplan, 2005: Further improvements to the Statistical Hurricane Intensity Prediction Scheme (SHIPS). *Wea. Forecasting*, **20**, 531–543, https://doi.org/10.1175/WAF862.1.

Didlake, A. C., and R. A. Houze, 2009: Convective-scale downdrafts in the principal rainband of Hurricane Katrina (2005). *Mon. Wea. Rev.*, **137**, 3269–3293, https://doi.org/10.1175/2009MWR2827.1.

Donelan, M. A., B. K. Haus, N. Reul, W. J. Plant, M. Stiassnie, H. C. Graber, O. B. Brown, and E. S. Saltzman, 2004: On the limiting aerodynamic roughness of the ocean in very strong winds. *Geophys. Res. Lett.*, **31**, L18306, https://doi.org/10.1029/2004GL019460.

Drennan, W. M., J. A. Zhang, J. R. French, C. McCormick, and P. G. Black, 2007: Turbulent fluxes in the hurricane boundary layer. Part II: Latent heat flux. *J. Atmos. Sci.*, **64**, 1103–1115, https://doi.org/10.1175/JAS3889.1.

Dunion, J. P., 2011: Rewriting the climatology of the tropical North Atlantic and Caribbean Sea atmosphere. *J. Climate*, **24**, 893–908, https://doi.org/10.1175/2010JCLI3496.1.

Fairall, C. W., E. F. Bradley, J. E. Hare, A. A. Grachev, and J. B. Edson, 2003: Bulk parameterization of air–sea fluxes: Updates and verification for the COARE algorithm. *J. Climate*, **16**, 571–591, https://doi.org/10.1175/1520-0442(2003)016<0571:BPOASF>2.0.CO;2.

Finocchio, P. M., and S. J. Majumdar, 2017a: The predictability of idealized tropical cyclones in environments with time-varying vertical wind shear. *J. Adv. Model. Earth Syst.*, **9**, 2836–2862, https://doi.org/10.1002/2017MS001168.

——, and ——, 2017b: A statistical perspective on wind profiles and vertical wind shear in tropical cyclone environments of the Northern Hemisphere. *Mon. Wea. Rev.*, **145**, 361–378, https://doi.org/10.1175/MWR-D-16-0221.1.

——, ——, D. S. Nolan, and M. Iskandarani, 2016: Idealized tropical cyclone responses to the height and depth of environmental vertical wind shear. *Mon. Wea. Rev.*, **144**, 2155–2175, https://doi.org/10.1175/MWR-D-15-0320.1.

Fischer, M. S., B. H. Tang, K. L. Corbosiero, and C. M. Rozoff, 2018: Normalized convective characteristics of tropical cyclone rapid intensification events in the North Atlantic and eastern North Pacific. *Mon. Wea. Rev.*, **146**, 1133–1155, https://doi.org/10.1175/MWR-D-17-0239.1.

Foerster, A. M., and M. M. Bell, 2017: Thermodynamic retrieval in rapidly rotating vortices from multiple-Doppler radar data. *J. Atmos. Oceanic Technol.*, **34**, 2353–2374, https://doi.org/10.1175/JTECH-D-17-0073.1.

Frank, W. M., and E. A. Ritchie, 1999: Effects of environmental flow upon tropical cyclone structure. *Mon. Wea. Rev.*, **127**, 2044–2061, https://doi.org/10.1175/1520-0493(1999)127<2044:EOEFUT>2.0.CO;2.

——, and ——, 2001: Effects of vertical wind shear on the intensity and structure of numerically simulated hurricanes. *Mon. Wea. Rev.*, **129**, 2249–2269, https://doi.org/10.1175/1520-0493(2001)129<2249:EOVWSO>2.0.CO;2.

Gao, S., S. Zhai, B. Chen, and T. Li, 2017: Water budget and intensity change of tropical cyclones over the western North Pacific. *Mon. Wea. Rev.*, **145**, 3009–3023, https://doi.org/10.1175/MWR-D-17-0033.1.

Hence, D. A., and R. A. Houze, 2008: Kinematic structure of convective-scale elements in the rainbands of Hurricanes Katrina and Rita (2005). *J. Geophys. Res.*, **113**, D15108, https://doi.org/10.1029/2007JD009429.

Hong, S.-Y., Y. Noh, and J. Dudhia, 2006: A new vertical diffusion package with an explicit treatment of entrainment processes. *Mon. Wea. Rev.*, **134**, 2318–2341, https://doi.org/10.1175/MWR3199.1.

Iacono, M. J., J. S. Delamere, E. J. Mlawer, M. W. Shephard, S. A. Clough, and W. D. Collins, 2008: Radiative forcing by long-lived greenhouse gases: Calculations with the AER radiative transfer models. *J. Geophys. Res.*, **113**, D13103, https://doi.org/10.1029/2008JD009944.

Jones, S. C., 1995: The evolution of vortices in vertical shear. I: Initially barotropic vortices. *Quart. J. Roy. Meteor. Soc.*, **121**, 821–851, https://doi.org/10.1002/qj.49712152406.

——, 2000: The evolution of vortices in vertical shear. II: Large-scale asymmetries. *Quart. J. Roy. Meteor. Soc.*, **126**, 3137–3159, https://doi.org/10.1002/qj.49712657008.

Juračić, A., and D. J. Raymond, 2016: The effects of moist entropy and moisture budgets on tropical cyclone development. *J. Geophys. Res. Atmos.*, **121**, 9458–9473, https://doi.org/10.1002/2016JD025065.

Knaff, J. A., C. R. Sampson, and M. DeMaria, 2005: An operational statistical typhoon intensity prediction scheme for the western North Pacific. *Wea. Forecasting*, **20**, 688–699, https://doi.org/10.1175/WAF863.1.

Komaromi, W. A., 2013: An investigation of composite dropsonde profiles for developing and nondeveloping tropical waves during the 2010 PREDICT field campaign. *J. Atmos. Sci.*, **70**, 542–558, https://doi.org/10.1175/JAS-D-12-052.1.

Kwon, Y. C., and W. M. Frank, 2008: Dynamic instabilities of simulated hurricane-like vortices and their impacts on the core structure of hurricanes. Part II: Moist experiments. *J. Atmos. Sci.*, **65**, 106–122, https://doi.org/10.1175/2007JAS2132.1.

Leppert, K. D., D. J. Cecil, and W. A. Petersen, 2013a: Relation between tropical easterly waves, convection, and tropical cyclogenesis: A Lagrangian perspective. *Mon. Wea. Rev.*, **141**, 2649–2668, https://doi.org/10.1175/MWR-D-12-00217.1.

——, W. A. Petersen, and D. J. Cecil, 2013b: Electrically active convection in tropical easterly waves and implications for tropical cyclogenesis in the Atlantic and east Pacific. *Mon. Wea. Rev.*, **141**, 542–556, https://doi.org/10.1175/MWR-D-12-00174.1.

Marín, J. C., D. J. Raymond, and G. B. Raga, 2009: Intensification of tropical cyclones in the GFS model. *Atmos. Chem. Phys.*, **9**, 1407–1417, https://doi.org/10.5194/acp-9-1407-2009.

Marks, F. D., Jr., R. A. Houze Jr., and J. F. Gamache, 1992: Dual-aircraft investigation of the inner core of Hurricane Norbert. Part I: Kinematic structure. *J. Atmos. Sci.*, **49**, 919–942, https://doi.org/10.1175/1520-0469(1992)049<0919:DAIOTI>2.0.CO;2.

Moeng, C.-H., 1984: A large-eddy-simulation model for the study of planetary boundary-layer turbulence. *J. Atmos. Sci.*, **41**, 2052–2062, https://doi.org/10.1175/1520-0469(1984)041<2052:ALESMF>2.0.CO;2.

Montgomery, M. T., and R. K. Smith, 2014: Paradigms for tropical cyclone intensification. *Aust. Meteor. Oceanogr. J.*, **64**, 37–66, https://doi.org/10.22499/2.6401.005.

Munsell, E. B., F. Zhang, and D. P. Stern, 2013: Predictability and dynamics of a nonintensifying tropical storm: Erika (2009). *J. Atmos. Sci.*, **70**, 2505–2524, https://doi.org/10.1175/JAS-D-12-0243.1.

Nguyen, L. T., and J. Molinari, 2012: Rapid intensification of a sheared, fast-moving hurricane over the Gulf Stream. *Mon. Wea. Rev.*, **140**, 3361–3378, https://doi.org/10.1175/MWR-D-11-00293.1.

Nolan, D. S., 2011: Evaluating environmental favorableness for tropical cyclone development with the method of point-downscaling. *J. Adv. Model. Earth Syst.*, **3**, M08001, https://doi.org/10.1029/2011MS000063.

——, and E. D. Rappin, 2008: Increased sensitivity of tropical cyclogenesis to wind shear in higher SST environments. *Geophys. Res. Lett.*, **35**, L14805, https://doi.org/10.1029/2008GL034147.

Onderlinde, M. J., and D. S. Nolan, 2014: Environmental helicity and its effects on development and intensification of tropical cyclones. *J. Atmos. Sci.*, **71**, 4308–4320, https://doi.org/10.1175/JAS-D-14-0085.1.

——, and ——, 2017: The tropical cyclone response to changing wind shear using the method of time-varying point-downscaling. *J. Adv. Model. Earth Syst.*, **9**, 908–931, https://doi.org/10.1002/2016MS000796.

Powell, M. D., 1990: Boundary layer structure and dynamics in outer hurricane rainbands. Part II: Downdraft modification and mixed layer recovery. *Mon. Wea. Rev.*, **118**, 918–938, https://doi.org/10.1175/1520-0493(1990)118<0918:BLSADI>2.0.CO;2.

Reasor, P. D., and M. D. Eastin, 2012: Rapidly intensifying Hurricane Guillermo (1997). Part II: Resilience in shear. *Mon. Wea. Rev.*, **140**, 425–444, https://doi.org/10.1175/MWR-D-11-00080.1.

——, M. T. Montgomery, F. D. Marks, and J. F. Gamache, 2000: Low-wavenumber structure and evolution of the hurricane inner core observed by airborne dual-Doppler radar. *Mon. Wea. Rev.*, **128**, 1653–1680, https://doi.org/10.1175/1520-0493(2000)128<1653:LWSAEO>2.0.CO;2.

——, R. Rogers, and S. Lorsolo, 2013: Environmental flow impacts on tropical cyclone structure diagnosed from airborne Doppler radar composites. *Mon. Wea. Rev.*, **141**, 2949–2969, https://doi.org/10.1175/MWR-D-12-00334.1.

Riemer, M., 2016: Meso-β-scale environment for the stationary band complex of vertically sheared tropical cyclones. *Quart. J. Roy. Meteor. Soc.*, **142**, 2442–2451, https://doi.org/10.1002/qj.2837.

——, and M. T. Montgomery, 2011: Simple kinematic models for the environmental interaction of tropical cyclones in vertical wind shear. *Atmos. Chem. Phys.*, **11**, 9395–9414, https://doi.org/10.5194/acp-11-9395-2011.

——, and F. Laliberté, 2015: Secondary circulation of tropical cyclones in vertical wind shear: Lagrangian diagnostic and pathways of environmental interaction. *J. Atmos. Sci.*, **72**, 3517–3536, https://doi.org/10.1175/JAS-D-14-0350.1.

——, M. T. Montgomery, and M. E. Nicholls, 2010: A new paradigm for intensity modification of tropical cyclones: Thermodynamic impact of vertical wind shear on the inflow layer. *Atmos. Chem. Phys.*, **10**, 3163–3188, https://doi.org/10.5194/acp-10-3163-2010.

——, ——, and ——, 2013: Further examination of the thermodynamic modification of the inflow layer of tropical cyclones by vertical wind shear. *Atmos. Chem. Phys.*, **13**, 327–346, https://doi.org/10.5194/acp-13-327-2013.

Rios-Berrios, R., and R. D. Torn, 2017: Climatological analysis of tropical cyclone intensity changes under moderate vertical wind shear. *Mon. Wea. Rev.*, **145**, 1717–1738, https://doi.org/10.1175/MWR-D-16-0350.1.

——, C. A. Davis, and R. D. Torn, 2018: A hypothesis for the intensification of tropical cyclones under moderate vertical wind shear. *J. Atmos. Sci.*, **75**, 4149–4173, https://doi.org/10.1175/JAS-D-18-0070.1.

Rogers, R., S. Chen, J. Tenerelli, and H. Willoughby, 2003: A numerical study of the impact of vertical shear on the distribution of rainfall in Hurricane Bonnie (1998). *Mon. Wea. Rev.*, **131**, 1577–1599, https://doi.org/10.1175//2546.1.

——, P. D. Reasor, and J. A. Zhang, 2015: Multiscale structure and evolution of Hurricane Earl (2010) during rapid intensification. *Mon. Wea. Rev.*, **143**, 536–562, https://doi.org/10.1175/MWR-D-14-00175.1.

Rotunno, R., and K. A. Emanuel, 1987: An air–sea interaction theory for tropical cyclones. Part II: Evolutionary study using a nonhydrostatic axisymmetric numerical model. *J. Atmos. Sci.*, **44**, 542–561, https://doi.org/10.1175/1520-0469(1987)044<0542:AAITFT>2.0.CO;2.

Simpson, R., and R. Riehl, 1958: Mid-tropospheric ventilation as a constraint on hurricane development and maintenance. *Tech. Conf. on Hurricanes*, Miami Beach, FL, Amer. Meteor. Soc., D4-1–D4-10.

Skamarock, W. C., M. L. Weisman, and J. B. Klemp, 1994: Three-dimensional evolution of simulated long-lived squall lines. *J. Atmos. Sci.*, **51**, 2563–2584, https://doi.org/10.1175/1520-0469(1994)051<2563:TDEOSL>2.0.CO;2.

Smith, R. K., and M. T. Montgomery, 2015: Toward clarity on understanding tropical cyclone intensification. *J. Atmos. Sci.*, **72**, 3020–3031, https://doi.org/10.1175/JAS-D-15-0017.1.

——, ——, and H. Zhu, 2005: Buoyancy in tropical cyclones and other rapidly rotating atmospheric vortices. *Dyn. Atmos. Oceans*, **40**, 189–208, https://doi.org/10.1016/j.dynatmoce.2005.03.003.

Sommeria, G., 1976: Three-dimensional simulation of turbulent processes in an undisturbed trade-wind boundary layer. *J. Atmos. Sci.*, **33**, 216–241, https://doi.org/10.1175/1520-0469(1976)033<0216:TDSOTP>2.0.CO;2.

Sprenger, M., and H. Wernli, 2015: The LAGRANTO Lagrangian analysis tool—Version 2.0. *Geosci. Model Dev.*, **8**, 2569–2586, https://doi.org/10.5194/gmd-8-2569-2015.

Stevenson, S. N., K. L. Corbosiero, and J. Molinari, 2014: The convective evolution and rapid intensification of Hurricane Earl (2010). *Mon. Wea. Rev.*, **142**, 4364–4380, https://doi.org/10.1175/MWR-D-14-00078.1.

Susca-Lopata, G., J. Zawislak, E. J. Zipser, and R. F. Rogers, 2015: The role of observed environmental conditions and precipitation evolution in the rapid intensification of Hurricane Earl (2010). *Mon. Wea. Rev.*, **143**, 2207–2223, https://doi.org/10.1175/MWR-D-14-00283.1.

Tang, B., and K. Emanuel, 2010: Midlevel ventilation's constraint on tropical cyclone intensity. *J. Atmos. Sci.*, **67**, 1817–1830, https://doi.org/10.1175/2010JAS3318.1.

——, and ——, 2012a: Sensitivity of tropical cyclone intensity to ventilation in an axisymmetric model. *J. Atmos. Sci.*, **69**, 2394–2413, https://doi.org/10.1175/JAS-D-11-0232.1.

——, and ——, 2012b: A ventilation index for tropical cyclones. *Bull. Amer. Meteor. Soc.*, **93**, 1901–1912, https://doi.org/10.1175/BAMS-D-11-00165.1.

——, R. Rios-Berrios, J. J. Alland, J. D. Berman, and K. L. Corbosiero, 2016: Sensitivity of axisymmetric tropical cyclone spinup time to dry air aloft. *J. Atmos. Sci.*, **73**, 4269–4287, https://doi.org/10.1175/JAS-D-16-0068.1.

Tao, D., and F. Zhang, 2014: Effect of environmental shear, sea-surface temperature, and ambient moisture on the formation and predictability of tropical cyclones: An ensemble-mean perspective. *J. Adv. Model. Earth Syst.*, **6**, 384–404, https://doi.org/10.1002/2014MS000314.

Wang, Y., and G. J. Holland, 1996: Tropical cyclone motion and evolution in vertical shear. *J. Atmos. Sci.*, **53**, 3313–3332, https://doi.org/10.1175/1520-0469(1996)053<3313:TCMAEI>2.0.CO;2.

Wernli, B. H., and H. C. Davies, 1997: A Lagrangian-based analysis of extratropical cyclones. I: The method and some applications. *Quart. J. Roy. Meteor. Soc.*, **123**, 467–489, https://doi.org/10.1002/qj.49712353811.

Willoughby, H. E., F. D. Marks, and R. J. Feinberg, 1984: Stationary and moving convective bands in hurricanes. *J. Atmos. Sci.*, **41**, 3189–3211, https://doi.org/10.1175/1520-0469(1984)041<3189:SAMCBI>2.0.CO;2.

Zawislak, J., and E. J. Zipser, 2014: A multisatellite investigation of the convective properties of developing and nondeveloping tropical disturbances. *Mon. Wea. Rev.*, **142**, 4624–4645, https://doi.org/10.1175/MWR-D-14-00028.1.

Zhang, F., and D. Tao, 2013: Effects of vertical wind shear on the predictability of tropical cyclones. *J. Atmos. Sci.*, **70**, 975–983, https://doi.org/10.1175/JAS-D-12-0133.1.